

# Ab-initio tree-tensor-network digital twin for quantum computer benchmarking in 2D

Daniel Jaschke<sup>1,2,3\*</sup>, Alice Pagano<sup>1,2,3</sup>, Sebastian Weber<sup>1,4</sup> and Simone Montangero<sup>1,2,3</sup>

<sup>1</sup>*Institute for Complex Quantum Systems, Ulm University, Albert-Einstein-Allee 11, 89069 Ulm, Germany*

<sup>2</sup>*Dipartimento di Fisica e Astronomia "G. Galilei" & Padua Quantum Technologies Research Center, Università degli Studi di Padova, Italy I-35131, Padova, Italy*

<sup>3</sup>*INFN, Sezione di Padova, via Marzolo 8, I-35131, Padova, Italy\**

<sup>4</sup>*Institute for Theoretical Physics III and Center for Integrated Quantum Science and Technology, University of Stuttgart, 70550 Stuttgart, Germany*

Large-scale numerical simulations of the Hamiltonian dynamics of a Noisy Intermediate Scale Quantum (NISQ) computer – a digital twin – could play a major role in developing efficient and scalable strategies for tuning quantum algorithms for specific hardware. Via a two-dimensional tensor network digital twin of a Rydberg atom quantum computer, we demonstrate the feasibility of such a program. In particular, we quantify the effects of gate crosstalks induced by the van der Waals interaction between Rydberg atoms: according to an  $8 \times 8$  digital twin simulation based on the current state-of-the-art experimental setups, the initial state of a five-qubit repetition code can be prepared with a high fidelity, a first indicator for a compatibility with fault-tolerant quantum computing. The preparation of a 64-qubit Greenberger-Horne-Zeilinger (GHZ) state with about 700 gates yields a 99.9% fidelity in a closed system while achieving a speedup of 35% via parallelization.

The present NISQ era of quantum computing poses extreme experimental, theoretical, and engineering challenges for all promising quantum computing platforms, being condensed matter or atomic-molecular-optical based ones [1–4]. Indeed, identifying the best approaches, engineering solutions, and optimizing strategies at the physical, logical and algorithmic levels is necessary to maximize the capability of NISQ computers and unlock the fault-tolerant scalable era of general-purpose quantum computing [5]. In the last two decades, these challenges have been mostly attacked at the level of few qubits, with impressive developments in, e.g., qubits and gate qualities [6–8]. However, the years ahead require achieving scalability and that will only be possible by understanding and characterizing the performances and limitations of the existing building blocks while functioning as one. For example, high-fidelity implementations will require taking into account also fast-decaying long-range interactions. Moreover, to go beyond NISQ, decoherence effects shall be mitigated by reducing quantum circuits depth while quantum error-correcting codes will come at the price of additional gates: all this confront the software stack with further challenges, e.g., to what degree the gates on logical qubits can run in parallel.

Here, we develop an efficient digital twin of a two-dimensional quantum processing unit (QPU) with access to a variety of compelling features, e.g., additional levels beyond the qubit states, long-range interactions, and decoherence effects. These features of a large-scale digital twin of the QPU will be fundamental to support the next decades of developments, e.g., comparable to the impact that optimal control simulations had on the development of high-fidelity single and two-qubit gates [8–10].

Via tensor network methods [11–14], we perform two-dimensional large-scale classical simulations of a quantum computer running non-trivial quantum algorithms; tensor network methods allow one to overcome the curse of the exponentially increasing Hilbert space [15]. We combine the digital twin with a customized compiler and demonstrate how together they identify limiting factors of current or future hardware. In this respect, the different topology and connectivity, e.g., 1-dimensional systems versus 2-dimensional ones, can lead to very distinct results in terms of the scaling of algorithms. We thus demonstrate how digital twins could guide the development of future quantum algorithm compilers and transpilers [16–18], specifically analyzing a Rydberg QPU in two dimensions.

Rydberg atoms trapped in optical tweezers represent one promising platform for realizing a quantum computer [19–25]. The Rydberg architecture has been impressively improved in various aspects over the last years and the execution of quantum algorithms of increasing complexity and circuit depth is in sight: recent Rydberg experiments have demonstrated two-qubit gate fidelities beyond 98% [26–29]. A key ingredient to increasing the final computation quality and the achievable circuit complexity is evidently the ability to run gates in parallel. Parallel gate execution requires an independent parallel control and addressing of each qubit, which has been recently demonstrated [30–35]. Understanding if and how an algorithm can be parallelized in the presence of long-range interactions, different connectivity, and spurious qubit crosstalks provides thus crucial insights to attack the next quantum computing engineering challenges. The building blocks to experimentally implement the protocol suggested in the following in this manuscript are available, foremost the CZ has been realized for example with  $^{87}\text{Rb}$  atoms [36].

To test the limits of the hardware on the digital twin,

\* Corresponding author: daniel-1.jaschke@uni-ulm.de

we analyze an algorithm that can be easily verified via the measurement statistics in an experiment, can be scaled with system size, is compatible with NISQ devices from the expected fidelity, and generates an amount of entanglement compatible with simulations on a classical computer. The preparation of large GHZ states fulfills these characteristics. Moreover, the GHZ state is becoming a standard benchmark of the ability to control highly non-classical properties of quantum hardware. Since the seminal demonstration of 14-qubit GHZ states in a trapped ion quantum computer [37], other platforms have accepted the challenge as well [38–40]. Recently, six-qubit GHZ states have been realized in a Rydberg quantum processor [41]. Therefore, this problem serves as an example of how to use the digital twin from the problem statement to the statistics of projective measurements comparable to an actual experimental setup.

The digital twin allows one to establish the optimal radius beyond which gates can run in parallel without significant crosstalk on the  $^{88}\text{Sr}$  Rydberg platform [36, 43, 44]. In particular, we characterize the trade-off between higher parallelization versus smaller errors due to crosstalk: on the one hand, a lower circuit depth comes with higher error rates induced by the Rydberg interaction; on the other hand, we pay for higher precision gates with larger circuit depths and an increasing vulnerability to decoherence. As sketched in Fig. 1a), we compile the circuit with a dedicated compiler *RydberGHZ-C* targeting the GHZ state in a two-dimensional geometry. Then, we use realistic and conservative parameters for the simulation of an  $8 \times 8$  strontium-88 setup [44], for example, taking into account long-range Rydberg interactions. For a 64-qubit GHZ state, we obtain a state infidelity of a  $10^{-2}$  level for the closed quantum system and controllable crosstalk. The circuit depth is only 15% above the theoretical minimum for a 2D square system with nearest-neighbor connectivity and the same gate set. Finally, we demonstrate an application of the digital twin on parallel GHZ states generation, e.g., encountered in the initial preparation of quantum error-correcting five-qubit repetition code [45–47].

The numerical workhorse behind the ab-initio Hamiltonian-based emulation of a parallel quantum computation is a tree tensor network (TTN) simulating a square lattice of qutrits taking into account the states  $|0\rangle$ ,  $|1\rangle$ , and the Rydberg state  $|r\rangle$  [48]. Within the family of tensor network algorithms [49–52], the TTN is a powerful ansatz for two-dimensional systems. The simulation of the system time evolution is implemented by exploiting recent progress in tensor network methods [11–14]: in particular, the time-dependent variational principle which supports the long-range interactions required for picturing crosstalk and the scheduling of parallel gates [11, 13]. On the one hand, the combination of the many-body simulations with optimal control results to include time-optimal gates and a compiler requires to master and merge all the existing state-of-the-art building blocks. On the other hand, exactly this overarch-

ing approach distinguishes it from independently carried out analysis by the insight that can be gained: with an equivalent size of 101 qubits, the digital twins sets the standard for emulating a QPU at the Hamiltonian level on a classical computer.

The structure of the manuscript is the following: we focus on the prospect of running quantum algorithms in parallel on the Rydberg platform by constructing a global GHZ state and preparing multiple GHZ states on five qubits in Sec. I. A detailed description of the Rydberg system including open quantum system effects follows in Sec. II. Afterward, we explain the technical aspects of the tensor network simulations in Sec. III and the RydberGHZ-C designed for the parallel GHZ preparation in Sec. IV. We conclude with a brief summary and outlook.

## I. PARALLEL QUANTUM ALGORITHMS

The digital twin relies on an ab-initio Hamiltonian description of the platform. We consider that there is the potential to study all qubit platforms in the way we demonstrate the simulations here for Rydberg atoms. The most challenging numerical aspects, i.e., the two-dimensional layout of superconducting hardware and the long-range interactions of trapped ions, are combined in the Rydberg platform. The two-dimensional structures in superconducting QPUs are continuously scaled up and achieve 127 qubits [53], which is already twice the size of the 64-qubit system studied here. Although trapped ions systems are one-dimensional, their strong long-range interactions allow an all-to-all connectivity [54] which can lead to a rapid growth of entanglement and the classical resources needed for the digital twin. In the following, we consider solely Rydberg systems, i.e., neutral atoms.

For the Rydberg platform, the physics required to understand the parallelization of the GHZ state preparation can be summarized according to Fig. 1. We focus on the crosstalk in a closed quantum system in this section and discuss open system effects in Sec. II. Figure 1a) shows a sketch of a  $4 \times 4$  setup of Rydberg atoms in optical tweezers; the lattice constant of the grid  $a$  introduces the first relevant length scale. Within the Rydberg blockade radius  $r_B$ , only a single atom can be excited to the Rydberg state due to the van der Waals interactions. We work at a fixed Rydberg blockade radius  $r_B = 4.98\mu\text{m} = 1.66a$  in accordance with the experimental parameters proposed in Ref. [44], which also provides the time-optimal CZ gate used in the simulation here as well as the parameters for a Strontium-88 setup; the pulse sequence for the time-optimal CZ gate stems from optimal control. On the one hand, the van der Waals interaction is giving rise to the Rydberg blockade which is exploited to implement an entangling gate between two atoms; on the other hand, the van der Waals interaction leads to possible crosstalk if multiple entangling gates act in parallel and atoms of two different CZ gates interact via van der Waals inter-

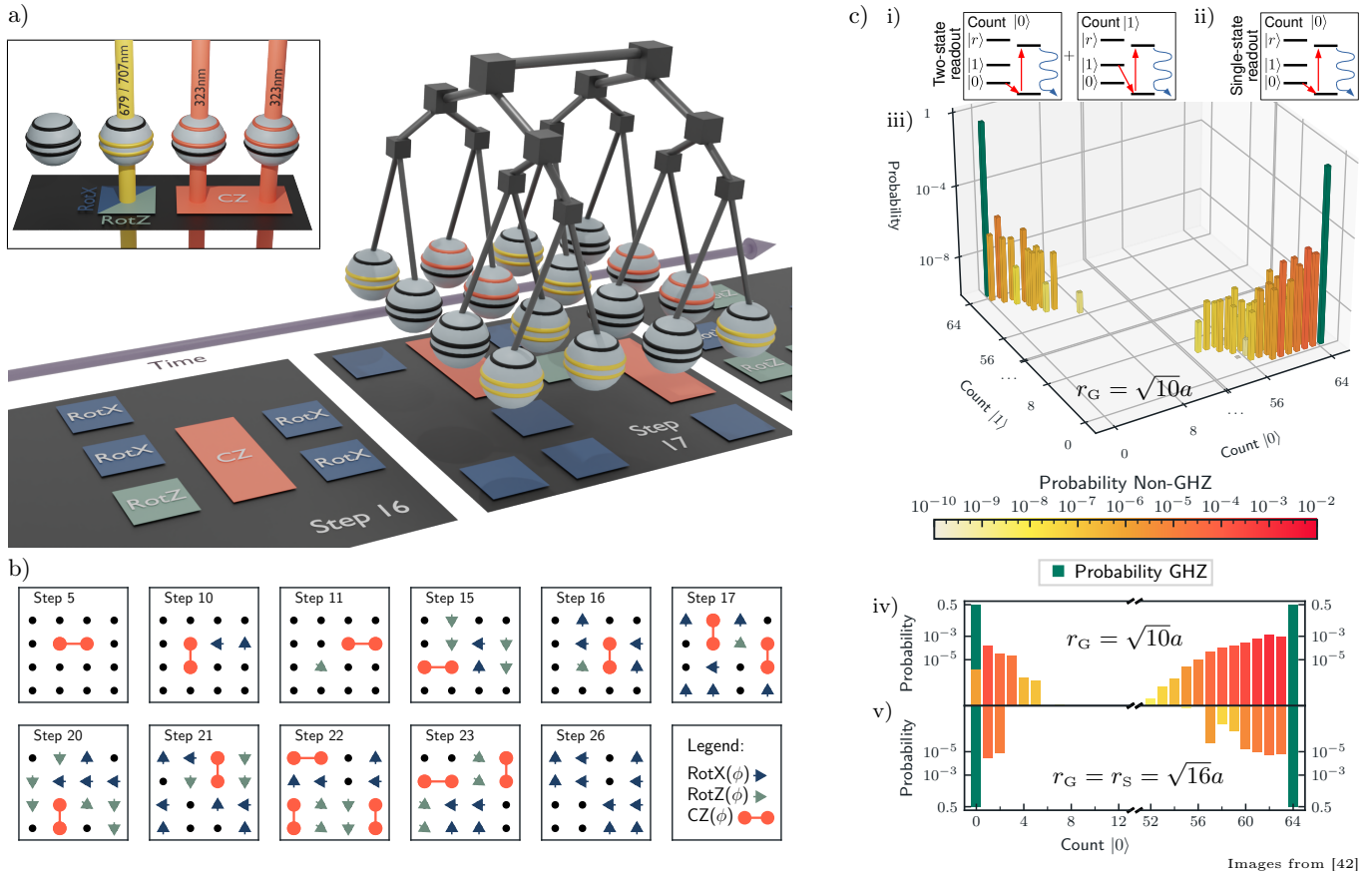


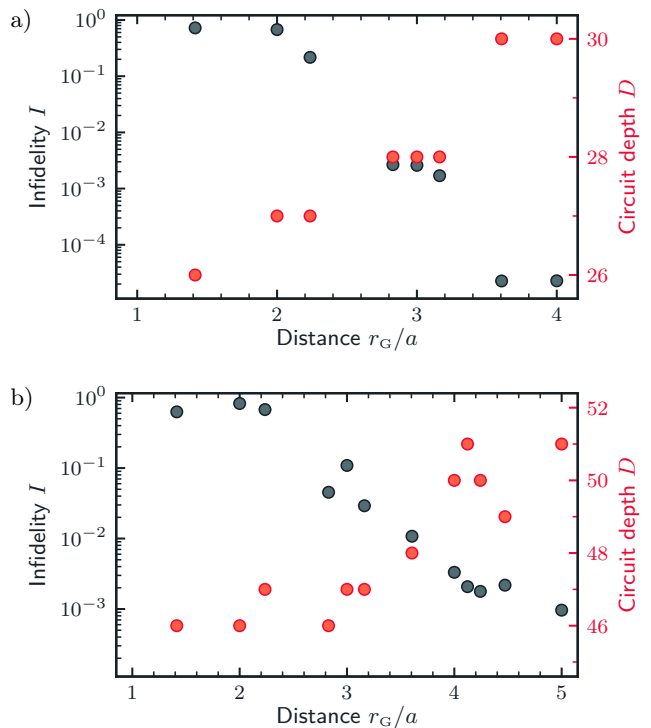
FIG. 1. a) *Rydberg quantum computer setup*: We simulate a square grid of  $^{88}\text{Sr}$  Rydberg atoms trapped in optical tweezers. In each step, a layer of parallel gates is applied: the controlled phase gates involve the strongly interacting Rydberg state  $|r\rangle$ , thus two of them applied simultaneously in close proximity introduce crosstalk errors. A tree tensor network (TTN) simulates the Rydberg atoms as qutrits (states  $|0\rangle$ ,  $|1\rangle$ , and  $|r\rangle$ ). The lasers, individually addressing the atoms, implement the single-qubit and two-qubit gates (inset). b) *Parallelization*: Selected quantum algorithm layers of the GHZ state preparation in terms of selected gates native to the Rydberg platform. Each square contains gates that are executed in parallel for a minimal distance between CZ gates  $r_G \geq 2a$ , where  $a$  is the lattice spacing. c) *Experimental measurement schemes*: Projective measurements for a perfect GHZ state yield a 50% probability of counting either exactly 64 qubits in the  $|0\rangle$  or  $|1\rangle$  state for an  $8 \times 8$  closed quantum system. We can choose between a two-state readout scheme in i) or a single-state readout scheme in ii), which both use an additional state. For  $r_G = \sqrt{10}$ , we compare the measurement statistics of readout scheme i) in iii) to readout scheme ii) in iv). We identify the states attributed to the GHZ state (in green) versus states introduced due to crosstalk (see color bar). As a consequence of a remaining population in the Rydberg state, the sum of qubits measured in  $|0\rangle$  and  $|1\rangle$  does not necessarily add up to one, showing the effect of the remaining population in the Rydberg state  $|r\rangle$ . In comparison,  $r_G = \sqrt{16}a$  limits the crosstalk to an acceptable amount as shown for the single-state readout scheme (see v) and is defined as the safe radius  $r_S$  to run gates in parallel.

actions. Consider as an example atoms A and B being the target of the first CZ gate and atoms C and D being the target of a second CZ gate; crosstalk arises if A or B interacts with atoms of the other gates, i.e., C and D, while both gates are driven at the same time. In contrast to the van der Waals interaction used to implement the CZ gate between A and B, additional atoms in the Rydberg state like C and D corrupt the pulse sequence and lead to what we refer to as crosstalk. Our compilation strategy considers this condition and allows one to specify the minimal radius  $r_G$  which the RydberGHZ-C and scheduler enforce between any two qubits participating in different entangling gates executed in parallel. We

focus on the radius  $r_G$  while the other length scales are kept constant. Finally, we are able to identify the radius  $r_S$  where the crosstalk is negligible in comparison to other errors and where the algorithm is safely executed in parallel, i.e., we establish a criterion on the fidelity of our state preparation. Figure 1b) presents the GHZ preparation for  $r_G = 2a$  on a  $4 \times 4$  square lattice for a subset of native gates of the Rydberg platform which are implemented for the digital twin. The radius  $r_G$  changes the circuit depth  $D$  and the fidelity via crosstalk, while we keep the lattice constant  $a$  and the Rydberg blockade radius  $r_B$  fixed. In the following paragraphs, we analyze these effects in detail.

Figure 1c) showcases a typical result enabled by the digital twin simulation: the effects of crosstalk errors as they become visible in projective measurements analog to an experimental setup. The fact of simulating qutrits allows one to explore different readout schemes either with a readout of both qubit states, see i) in Fig. 1c), or a single-state readout scheme where we choose the  $|0\rangle$  state, see ii). For each measurement of the  $|0\rangle$  or  $|1\rangle$  state, one needs to transfer the corresponding state to an additional state for readout, e.g., to the ground state of the optical qubit. A single-state readout scheme, e.g., of state  $|0\rangle$ , avoids the additional overhead of transferring the second state  $|1\rangle$  also to state for the readout and measuring it. The sum along the axis «Count  $|1\rangle$ » of the histogram iii) for the two-state readout leads to the histogram iv) of the single-state readout. The sum of the probabilities along one axis underlines how the readout schemes differ in information: counting only the number of qubits in  $|0\rangle$ , the state  $|11\dots 11\rangle$  originating in the GHZ state is indistinguishable from the state  $|11\dots 11r\rangle$ , which has an error due to a remaining population in the  $|r\rangle$  state. In the example of Fig. 1c), this fraction is below  $10^{-5}$ . When comparing the probability bars representing errors is evident as the bars differ by two orders of magnitude, i.e., up to  $10^{-3}$  errors for  $r_G = \sqrt{10}a$  versus  $10^{-5}$  for  $r_G = \sqrt{16}a$ . The probabilities for this set of states shown in the histogram are extracted directly from the TTN by sampling 1,000,000 projective measurements. For both  $r_G = \sqrt{10}a$  and  $r_G = \sqrt{16}a$ , the samples cover at least 99.945% of the probability, i.e., a single measurement appears with at most 0.055% probability not in the data shown; these statistics can be directly compared to experiments. Although simulations of projective measurements are possible as shown in Fig. 1c), we concentrate in the remainder on the infidelity which is more accessible in its interpretation as a single number.

Figure 2 shows the change in the circuit depth  $D$  and the infidelity  $I$  of the algorithm for preparing a global GHZ state as a function of the radius  $r_G$ . The fidelity of the algorithm  $F$  is defined as the state fidelity  $F = |\langle\psi(\tau)|\psi_{\text{GHZ}}\rangle|^2$  at the end of the algorithm at time  $\tau$ ; the infidelity is  $I = 1 - F$ . The total time of the complete algorithm is  $\tau = D \cdot 122\text{ns}$ , which is the product of the circuit depth  $D$  times the 122ns pulse time per gate, and the circuit depth  $D$  depends itself on the compiler setting and system size. The circuit is generated with the RydberGHZ-C compiler targeting directly the Rydberg platform. On the one hand, the circuit depth drops, e.g., from over 51 to 46 while decreasing the distance  $r_G$  from  $\sqrt{25}a$  to  $\sqrt{2}a$  for the  $8 \times 8$  square lattice. On the other hand, we observe that the infidelity changes by more than two orders of magnitude while changing  $r_G$ . This change in infidelity is due to the Rydberg interaction decaying with a power of six, especially for the  $8 \times 8$  grid where we have the bigger number of CZ gates  $n$ . The overall fidelity  $F$  depends on the number of CZ gates  $n$ , therefore we define the average as  $\mathcal{F}_\circ = F^{1/n}$ . For the



Images from [42]

FIG. 2. Measuring the effect of controlled phase gates executed in parallel in a closed quantum system. The infidelity  $I$  decreases towards larger circuit depth  $D$  for the GHZ state preparation. a) For the  $4 \times 4$  grid, we identify a clear jump for distances  $r \geq 2$ , which allows reducing the circuit depth by more than six percent allowing an infidelity of a  $10^{-3}$  level. b) For the  $8 \times 8$  grid, larger distances have to be considered to go to a fidelity of the  $10^{-2}$  level at  $r_G \geq 4a$ . A gain in circuit depth of 35% is possible in comparison to a circuit without parallel CZ gates.

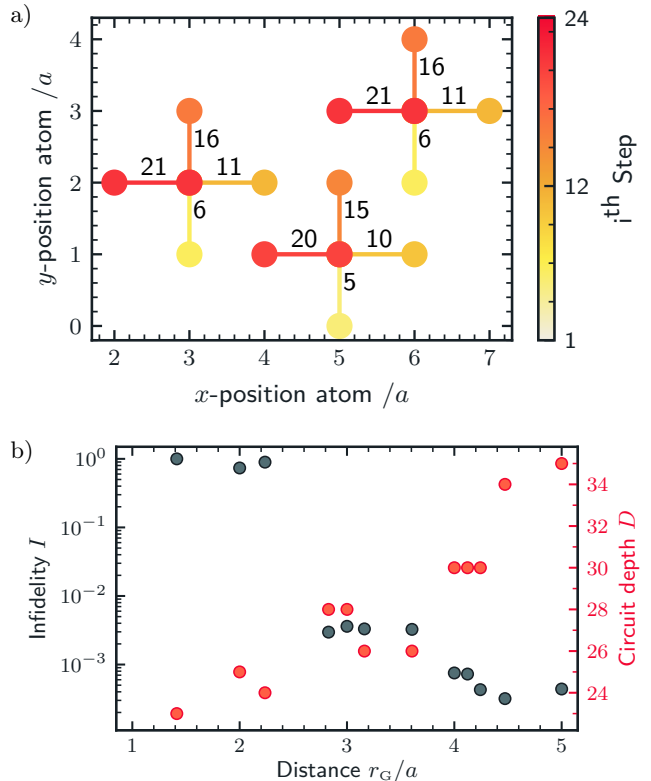
largest values of  $r_G$  shown in Fig. 2, the error is driven by small numerical artifacts always remaining in an optimized pulse sequence, i.e., the value of  $\mathcal{F}_\circ$  is in good agreement with the Bell state fidelity for a single gate of the protocol for the closed system from Ref. [44].

We now choose the radius  $r_G = r_s$  for a safely executed algorithm as  $r_s(L=4) = \sqrt{8}a$  and  $r_s(L=8) = \sqrt{16}a$ . In Sec. II on the Rydberg model, we show that the infidelity of the order of  $10^{-3}$  introduced in this scenario for a  $4 \times 4$  grid is below the largest errors of the order of  $10^{-2}$  introduced by decay from the Rydberg state. The same argument holds for an infidelity of the  $10^{-2}$  level for an  $8 \times 8$  system. In summary, Fig. 2 demonstrates that we identify the errors originating from parallel CZ gates on a Rydberg quantum computer; the ideal setting for the system is  $r_s(L=4) = \sqrt{8}a$  and  $r_s(L=8) = \sqrt{16}a$ , which leads to a tolerable loss in fidelity in comparison to a circuit serial in the CZ gates. We point out the reduction of the circuit depth by 35% for the  $8 \times 8$  system from a circuit depth 78 without any CZ gates in parallel to a circuit depth of 50, see Sec. IV for details. Meanwhile, the

effect in the  $4 \times 4$  system is almost negligible and reduces the circuit depth from 30 to 28 or about 7%, showing as expected a favorable scaling with the system size. In Sec. II, we prove that reducing the circuit depth and running gates in parallel allows one to minimize the overall error from crosstalk and open system effects caused by imperfections in the trapping of the atoms.

We now move on to the second example, which gives an outlook of parallel circuits beyond the NISQ applications: to the implementation of quantum error-correcting codes [47, 55]. We construct a five-qubit repetition code encoding one logical qubit into five physical qubits on a square lattice, which allows one to detect bit-flip errors. Each logical qubit can be implemented with one physical qubit and its four nearest neighbors. A repetition code needs to prepare the initial state  $|\psi\rangle = \alpha|0\rangle + \beta|1\rangle$  of each qubit in the algorithm into the logical qubit  $|\Psi\rangle = \alpha|00000\rangle + \beta|11111\rangle$ . Without loss of generality, we assume  $\alpha = \beta = 1/\sqrt{2}$  and a product state between the logical qubits. The preparation of the logical qubits can be parallelized to a greater extent than the preparation of the global GHZ state on the complete lattice: the first CZ gate of the global GHZ state has always to run in serial, i.e., there is only one option for the control qubit of the first CZ gate; in contrast, this preparation of multiple local GHZ states can have parallel gates from the first CZ gate on. We have the option of a dense filling in the two-dimensional geometry or leaving additional physical qubits unused, i.e., auxiliary qubits in applications, between the logical qubits. We choose the first option as the denser the packing is the more difficult the handling of crosstalk is.

Figure 3a) presents an example of the circuit for three logical qubits in the dense filling scheme; three logical qubits fit on a 16-site TTN. The binary TTN requires the number of sites to be a power of two; additional sites inserted to reach the next power of two do not affect the simulation, i.e., are in the ground state and never addressed by a laser. Each TTN site is still modeled as a qutrit. The setup allows one to repeat the analysis of the final fidelity as a function of  $r_G$  in this scenario, see Fig. 3b). We want to ensure that one can reach the same level of fidelity as in the global GHZ state, which is chosen with regard to error sources from open quantum systems; ideally, we can use the same distance  $r_s$  than before to reach the same or a better infidelity. We confirm the radius  $r_s(L=4) = \sqrt{8}a$  for a safe execution of the 15-qubit simulation of three logical qubits, which reaches an infidelity of  $10^{-3}$ , which can be improved further by one order of magnitude when increasing the radius further. Similarly, we observe  $r_s(L=8) = \sqrt{16}a$  for the 60-qubit simulation with twelve logical qubits reaching an infidelity of a  $10^{-2}$  level.



Images from [42]

FIG. 3. *Parallel initialization for quantum error-correcting codes.* a) Parallel example algorithm for preparing three logical qubits of a five-qubit repetition code; links of the same color refer to CZ gates executed in parallel in the same layer. The underlying TTN has sixteen sites. The preparation requires 24 layers in total. The steps indicated by the color map depend on  $r_G$ , which is set to  $r_G = 2a$  for this circuit. b) The infidelity  $I$  of GHZ state preparation for each logical qubit improves for larger radii  $r_G$  and circuit depths  $D$ .

## II. MODELING $^{88}\text{Sr}$ QUANTUM COMPUTERS ON TWO-DIMENSIONAL GRIDS

The Rydberg quantum processor analyzed here assumes the following characteristics: the atoms are trapped by optical tweezers in a two-dimensional grid; it is possible to individually address the neutral atoms, e.g., to drive the transition for the implementation of single-qubit rotation gate  $R_X$  or the transition to the Rydberg state for entangling two-qubit gates. The individual addressing of atoms allows one to group several single-qubit gates and two-qubit gates together into groups, where each group of gates can be executed at the same time. The strong interaction between the atoms within the Rydberg blockade radius affects the fidelity of executing controlled-phase gates in parallel.

We tailor the Hamiltonian towards an implementation with strontium-88 atoms, where the two-qubit states are encoded into the fine-structure qubit  $|0\rangle = |5^3P_0\rangle$  and  $|1\rangle = |5^3P_2\rangle$ ; the Rydberg state  $|r\rangle = |60^3S_1, m_J = 1\rangle$  is

required to implement the controlled-phase gate. Overall, the Hamiltonian  $H_{\text{Ryd}}$  and parameters follow Ref. [44] and consists of an idealized three-level system of

$$\begin{aligned}
H_{\text{Ryd}} = & \sum_{j,k} \Omega_{j,k}^x(t) \sigma_{j,k}^x + \Omega_{j,k}^z(t) \sigma_{j,k}^z \\
& + \sum_{j,k} (\Omega_{j,k}^R(t) |r\rangle \langle 1| + h.c.) \\
& + \sum_{j,k} \sum_{j',k'} V(j,k,j',k') n_{j,k} n_{j',k'}, \quad (1)
\end{aligned}$$

where the qubits in the two-dimensional grid are indexed with  $j$  and  $k$ . The Hamiltonian contains both, an effective Hamiltonian for implementing single-qubit gates and couplings to the interacting Rydberg states for the implementation of the two-qubit CZ gates. The effective Hamiltonian for the single-qubit gates uses the Pauli matrices  $\sigma^x = |0\rangle \langle 1| + |1\rangle \langle 0|$  for rotation-x gates of an arbitrary angle and the  $\sigma^z = |0\rangle \langle 0| - |1\rangle \langle 1|$  for rotation-z gates of an arbitrary angle. The single-qubit gates are driven by the corresponding time-dependent effective pulses  $\Omega^x$  and  $\Omega^z$ , respectively. The single-qubit gates are executed with high fidelity with respect to other error sources and are not the leading source of error [29]. The transition between the states  $|1\rangle$  and  $|r\rangle$  is driven by a single-photon transition and represented in the Hamiltonian by the Rabi frequency  $\Omega^R$  and the transition  $|r\rangle \langle 1|$  and  $|1\rangle \langle r|$ . The Rydberg interaction is modeled via the interaction operator  $n = |r\rangle \langle r|$  and a van der Waals interaction, where the strength depends on the distance  $d$  as

$$V(j,k,j',k') = \frac{-C_6}{d^6}, \quad (2)$$

where  $d = \sqrt{(x_j - x_{j'})^2 + (y_k - y_{k'})^2}$ . To allow for arbitrary lattice structures, the position of the qubit labeled with the indices  $(j,k)$  is  $(x_j, y_k)$ . The coefficient  $C_6$  describes the strength of the van der Waals interactions [44]. This decaying interaction leads to the Rydberg blockade radius [56, 57], in which more than one excitation to the Rydberg state is prevented: the transition from one excitation to two excitation is off-resonant due to an additional energy shift. The Rydberg state is used for the implementation of two-qubit gates and has an immediate effect on the crosstalk of two gates running in parallel. The Hamiltonian of Eq. (1) is sufficient to implement a universal gate set consisting of rotation-x, rotation-z, and CZ gates.

Finally, we include a Lindblad description of the system introducing a decay of the Rydberg state  $|r\rangle$  for the analysis provided later in this section; as a starting point, we are interested in how much our fidelity decreases under the assumption that all decays end up in states outside our computational space, i.e., the worst-case scenario. Therefore, we include a non-Hermitian part to the Hamiltonian with the Lindblad operator  $L_{\text{decay}} = |d\rangle \langle r|$  analog to quantum trajectories [58, 59], where  $|d\rangle$  is any

dark state outside the computational states. We do not aim to retrieve  $|d\rangle$  and re-introduce it into the computational states. We obtain for the open quantum system

$$H_{\text{OQS}} = H_{\text{Ryd}} - i\gamma \sum_{j,k} |r\rangle \langle r|_{j,k}. \quad (3)$$

From all the possible error sources, the decay from the Rydberg state is the most important source of error for a single CZ gate [43, 44]. We also choose the conservative estimate of  $1/\gamma = 50\mu\text{s}$  for the decay time from Ref. [44].

In the following, we show that the remaining population in the Rydberg state quantifies the crosstalk and can serve as an indicator of the fidelity of the state preparation. The remaining population in the Rydberg state is

$$P_{\text{R}} = \sum_{j,k} \langle n_{j,k}(t = \tau) \rangle, \quad (4)$$

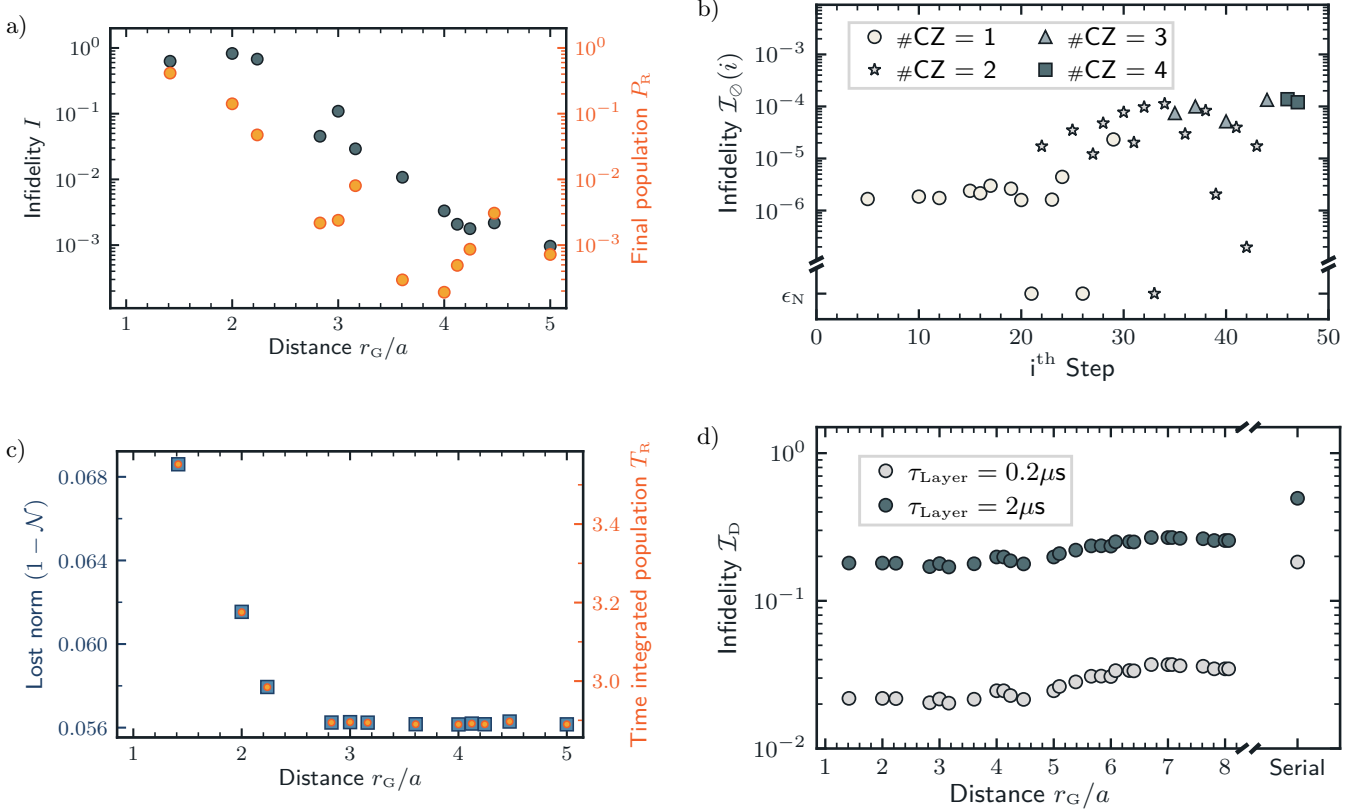
where we refer to the total time of the algorithm as  $\tau$ . The integrated time in the Rydberg state  $T_{\text{R}}$  is of interest when considering the open quantum system with decay from the Rydberg state. Without crosstalk, the time  $T_{\text{R}}$  in the Rydberg state and final population in the Rydberg state  $P_{\text{R}}$  depend only on the number of CZ gates; we expect the same behavior if the crosstalk is low enough. Therefore,  $T_{\text{R}}$  and  $P_{\text{R}}$  have a lower bound which also cannot be improved by optimizations, where  $T_{\text{R}}$  relates to Eq. (3). We define the integrated time in the Rydberg state as

$$T_{\text{R}} = \sum_{j,k} \int_0^\tau dt \langle n_{j,k}(t) \rangle, \quad (5)$$

where the time  $T_{\text{R}}$  connects directly to the probability of loss from the Rydberg state to a state outside of the computational space; this fraction of states identified by the lost norm is accounted for with a fidelity of zero.

With these observables, we analyze the choice of the minimal radius of  $r_{\text{G}}$  and to which extent we trade a better fidelity for a larger circuit depth. The minimal radius  $r_{\text{G}}$  describes the minimal distance between any two qubits of different CZ gates executed in parallel, e.g., a distance of  $r_{\text{G}} = 2a$  in Fig. 1a). We recall the dependency of the fidelity and the minimal radius  $r_{\text{G}}$  for entangling gates running in parallel discussed in Fig. 2, and we move towards looking at measurement specific to the Rydberg state of our platform in the next paragraph.

We observe that the parallel execution of CZ gates leads to a remaining population in the Rydberg state  $P_{\text{R}}$  as the gate is designed for serial use, i.e., the laser pulse used to drive the gate has been engineered for two perfectly isolated Rydberg atoms. In contrast, the system encounters four additional two-body interactions with interaction strengths depending on the positions of the atoms when running two CZ gates close to each other; then, the pulse sequence fails to perfectly reproduce the CZ gates. The remaining population in the



Images from [42]

FIG. 4. *Rydberg measurements for GHZ state preparation executed in parallel on  $8 \times 8$  systems.* a) We consider the populations in the Rydberg state for the final state of a closed system. Running parallel gates close to each other results in a large population in the Rydberg state, which causes an increase of the infidelity. b) We measure the infidelity after the application of each parallel layer and calculate the average error per CZ in one layer, i.e.,  $\mathcal{I}_\circ(i) = \mathcal{I}(i)^{-n}$  for  $n$  CZ in the  $i^{\text{th}}$  layer. Three data points cannot be captured by the numerical precision  $\epsilon_N$  of the simulation and appear on the  $y$ -axis as  $\epsilon_N$ . c) The open quantum system causes a finite loss of norm and time-integrated Rydberg population  $T_R$  because the execution of CZ gates temporarily populates the Rydberg state. But  $T_R$  becomes even larger at small radii  $r_G$  due to permanent Rydberg populations related to running parallel CZ gates in proximity to each other. d) The estimate for the infidelity introduced due to dephasing shows a jump of one order of magnitude for the serial circuit as well as for the comparison between the two scenarios with different layer durations  $\tau_{\text{Layer}}$ .

Rydberg state  $P_R$  presents a path to measure the effects of crosstalk and is shown in Fig. 4a). We employ the fact that  $|r\rangle$  is solely used for the gate implementation. Therefore, the measurement of the population in the Rydberg state is experimentally possible: after a readout of the qubit states  $|0\rangle$  and  $|1\rangle$  the probability remains below 1, which is one way to estimate the population in the Rydberg state  $|r\rangle$  and related losses. This two-state readout scheme can be implemented via an additional state, see Fig. 1c)i).

The digital twin allows one to evaluate which layers contribute the most to the final infidelity. Figure 4b) refines the average infidelity per CZ gate on the level of the  $i^{\text{th}}$  parallel layer for a closed quantum system, i.e.,  $\mathcal{I}_\circ(i)$ . The underlying average gate fidelity of the CZ gate is optimized up to  $\mathcal{F}_{\text{CZ}} = 99.99983\%$  and represents a meaningful reference value for  $1 - \mathcal{I}_\circ(i)$ . Although the error depends on the distances of parallel gates, we inter-

pret the trend to higher errors at the end of the circuit as a sign that errors propagate, e.g., a small population in the Rydberg state from a previous layer for the control qubit of the CZ gate affects the next layer. A difference between the system sizes is the number of previous errors that can affect CZ gates at a later stage, i.e., the paths for executing consecutive CZ gates in the  $8 \times 8$  grid are longer than in the  $4 \times 4$  grid, which is another reason for smaller average fidelities  $\mathcal{F}_\circ$  for the  $8 \times 8$  grid, in addition to running a greater fraction of CZ gates in parallel.

The accumulated infidelity  $I$  due to the crosstalk of the parallel algorithm has to be compared to other experimentally relevant sources of error. The decay from the Rydberg state has been identified as the major source of error for single-qubit and two-qubit gates [43, 44]. We assume the worst-case scenario that any decay from the Rydberg state  $|r\rangle$  leaves our computational basis of the states  $|0\rangle$ ,  $|1\rangle$ , and  $|r\rangle$ . The non-Hermitian version of

the Hamiltonian  $H_{\text{oqs}}$  in Eq. (3) describes this scenario of an open quantum system; the remaining norm  $\mathcal{N}$  of the state can be directly multiplied with the final fidelity to obtain the average fidelity of any quantum algorithm. For the square lattice with 16 qubits in total, we obtain a loss of norm in the order of  $1.4 \cdot 10^{-2}$ , i.e., a final fidelity of about 98.6% in the limit of large  $r_G$  assuming an otherwise perfect circuit. The lost norm is a good approximation of the infidelity, because the decay is the leading source of error for large radii  $r_G$ . Therefore, the error originating from crosstalk with  $r_G(L=4) = \sqrt{8}a$  below the order of  $3 \cdot 10^{-3}$  or less is negligible. We show the data for 64 qubits in Fig. 4c), where the fidelity drops to about 94.4%, i.e., an infidelity on the  $5.6 \cdot 10^{-2}$  level. We point out that increasing the radius  $r_G(L=8)$  beyond  $\sqrt{9}a$  in the regime of high fidelities leaves the loss in norm unchanged. Recall that the Lindblad operator acts on the state  $|r\rangle$ , which is the only state contributing to this loss in norm and we can demonstrate this connection by measuring  $T_R$ , i.e., the integrated population in the state  $|r\rangle$  for all qubits during the complete evolution, as shown in the right y-axis of Fig. 4c). For the same system size, we reach infidelities below  $5 \cdot 10^{-3}$  at  $r_G = \sqrt{16}a$  and therefore we set  $r_s = \sqrt{16}a$  as the error from the decay is dominating over the error from the crosstalk.

The challenge of conserving coherence in the quantum system is not reflected in the non-Hermitian Hamiltonian of Eq. (3), i.e., the open system term introduced with the decay does not favor circuits with shorter total time as one expects for the actual hardware. After the leading contribution of decay from the Rydberg state, the next relevant term stems from the fluctuations around the magic trapping condition [60, 61], which lead to decoherence, especially in the case of the GHZ state. In principle, perfect magic trapping is designed so that all three levels pick up the same phase and dephasing is eliminated. However, the magic trapping condition is never met perfectly in an experimental realization, e.g., because of field noise. We include this effect a posteriori into the results and consider how the decoherence time  $T_2 = 10\text{ms}$  affects the fidelity over the time  $t$ . The fidelity between a GHZ state of  $n$  qubits exposed to dephasing and a perfect GHZ state is

$$\mathcal{F}_D(t) = \frac{1}{2} + \frac{1}{2} \exp\left(-\frac{n \cdot t}{T_2}\right). \quad (6)$$

To include this effect in our estimate, we approximate that this decoherence affects each qubit starting with their first  $R_x(\phi)$  gate; to simplify the estimate, we neglect an additional treatment of the  $|r\rangle$  state as it appears only in a limited fraction of steps while applying the CZ gates. The pulse time for a CZ is  $0.122 \mu\text{s}$  and we choose the amplitudes for the single-qubit gates to match the time of the CZ gate. Recall that the qubit is encoded into the fine-structure qubit and thus single-qubit gate within  $0.122 \mu\text{s}$  are possible because of the strong Raman transition. However, this duration of the pulses neglects

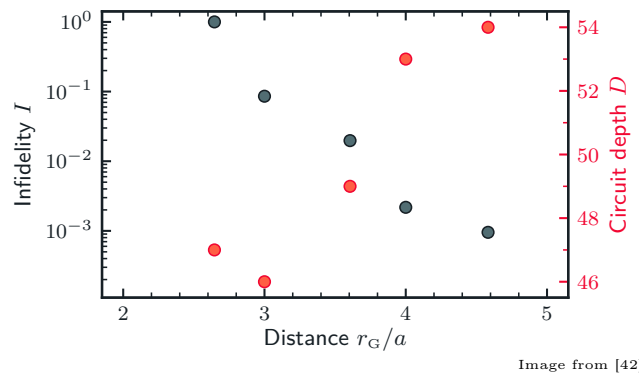


FIG. 5. Hexagonal lattices with  $8 \times 8$  Rydberg atoms. Infidelities  $I$  for the GHZ state preparation on a hexagonal lattice of a closed quantum system.

intermediate steps required between layers. Therefore, we follow two scenarios: the first scenario runs one layer every  $0.2 \mu\text{s}$  allowing for a gap after each pulse, and the more conservative second scenario with one layer every  $2 \mu\text{s}$ , e.g., including the possibility to move the addressing laser beams to different atoms between layers. Figure 4d) proves the need to parallelize the circuit. For both serial circuits and the parallel circuits with  $\tau_{\text{Layer}} = 2 \mu\text{s}$ , the decoherence is the leading source of error, i.e., even more important than decay from the Rydberg state. All of the circuits with  $\tau_{\text{Layer}} = 0.2 \mu\text{s}$  with parallel local gates bring the decoherence error below the level of the decay from the Rydberg state. The parallel circuits fluctuate due to the freedom of the scheduler, but the data suggests a trend towards higher errors from decoherence for larger circuit depths  $D$ . There are no possible distance in an  $8 \times 8$  system beyond  $r_G/a > \sqrt{74} = \sqrt{7^2 + 5^2} \approx 8.6$  which still have parallel gates; but in general, the serial case is with  $r_G/a = \infty$ .

Rydberg atoms are able to implement other lattice layouts than the square lattice, e.g., a hexagonal lattice. Although a hexagonal lattice has advantages in terms of connectivity, the parallelization of gates is actually more subtle due to the denser packing of the atoms in the lattice. For example, the area of a rectangle containing the Rydberg atoms of an  $8 \times 8$  hexagonal lattice is ten percent smaller than the area of the square containing  $8 \times 8$  atoms of a square lattice. The denser packing leads to the fact that more atoms are within the Rydberg blockade radius and parallelization is more restricted. Figure 5 provides an impression of the infidelity as a function of  $r_G$  in the hexagonal lattice layout. Overall, we reach similar fidelities than in the square lattice; the circuit depths  $D$  tend to be higher, while the  $r_G$  has the same effect on the infidelity. For example, a  $10^{-2}$  infidelity is reached in both layouts for  $3a < r_G < 4a$ .

Altogether, the combination of the parallel GHZ state preparation with the characteristics of the specific Rydberg setup allow us to obtain detailed insights, e.g., experimentally feasible measurements to characterize the



error of crosstalk or open system effects, and explore the consequences of different lattice layouts. Although the infidelity estimated for the decoherence fluctuates due to different scheduling, a comparison to the serial circuit shows the necessity to run algorithms in parallel and minimize the circuit depth as long as the crosstalk is controllable.

### III. TENSOR NETWORK SIMULATIONS

The digital twin is based on the tensor network simulations: here, we employ a binary TTN based on the software framework *Quantum TEA* [14, 48, 62, 63] and account for the two-dimensional architecture of the Rydberg array via the Hilbert curve mapping: the Hilbert curve maps a square lattice into a one-dimensional system and is in many scenarios favorable in comparison to other schemes [64]. Although the TTN is better suited for the two-dimensional system than a matrix product state, we still require a mapping and an ordering with a single index to label the leaves of the tree network. We display the original  $4 \times 4$  lattice before its mapping and the tree network in Fig. 1a). The time evolution is executed via the time-dependent variational principle [11, 13] and a two-tensor update, supporting long-range interactions required for the Rydberg interactions in Eq. (1). Due to the underlying two-dimensional grid and mapping with the Hilbert curvature, the Hamiltonian is described via a tensor product operator, i.e., a set of two-body interactions [65], and the number of two-body interaction terms grows as we increase the radius of Rydberg interactions that should be included. In the limit of an all-to-all interaction, the number of terms in the tensor product operator representing the Hamiltonian scales quadratically with the number of atoms. The translation of the gate sequence into the time evolution is split into each parallel layer to simplify the control of the time-dependent parameters. For example, the time-dependent laser-driving from Eq. (1) are set to zero for atoms not involved in any gate in the specific layer; atoms involved in a gate have exactly one out of  $\Omega^x$ ,  $\Omega^z$ , and  $\Omega^R$  turned on for their layer as each of them drives a different gate. The local gates are implemented as square pulses, the  $CZ(\phi)$  gate as described in Ref. [44].

Tensor network simulation presents a classical path toward many-body quantum simulations due to an entanglement-driven approximation: the simulation can become exact at a certain bond dimension  $\chi$  controlling the maximal amount of bipartite entanglement given by the Hilbert space or if the relevant quantum state does not exceed the entanglement that can be described with  $\chi$ . The GHZ state of our algorithm represents such a state with a low bond dimension, i.e., the state can be written with  $\chi = 2$ . Although we pick up additional entanglement due to imperfections of the gates, the target state represents the ideal playground to exploit tensor network in this scenario of providing results of a quan-

tum computer up to the pulse level. We recall that even the  $4 \times 4$  grid of the three-level system corresponds to an equivalent of simulating about 25 qubits. The square lattice of  $8 \times 8$  qutrits is equivalent to about 101 qubits and beyond the reach of exact methods and their upper limit of around 45 qubits [15, 66].

The long-range interactions of the Rydberg atoms play a crucial role. Therefore, we include more than the nearest-neighbor interactions at distances  $a$ , which are required for the CZ gate in  $x$ - and  $y$ -direction. We incorporate additional interactions depending on the radius  $r_G$  for running two CZ gates in parallel: interactions up to  $r_H = r_G + d_{\text{offset}}$  are included. Therefore, the computational effort increases for large  $r_G$  with respect to the number of terms in the Hamiltonian and the total number of time steps. The latter is induced by larger circuit depths. Due to the possibility of the remaining population in the Rydberg state  $|r\rangle$ , we are required to keep all interactions up to the radius  $r_H$ . This required range of interaction in the Hamiltonian is a direct consequence of Eq. (2) and the Rydberg blockade radius.

In summary, there are three crucial parameters for the convergence study presented in Tab. I, i.e., the bond dimension  $\chi$ , the time step  $dt$  of the evolution, and the range of interactions  $r_H$  included in the Hamiltonian, where  $r_H = r_G + d_{\text{offset}}$  is tuned via  $d_{\text{offset}}$ . To prove convergence, we validate the infidelity of the final states obtained by two different parameters  $p_1$  and  $p_2$  for either  $\chi$ ,  $dt$ , or  $d_{\text{offset}}$  and their effect on the fidelity with the perfect GHZ state, i.e.,

$$\mathcal{C}(p_1, p_2) = 1 - |\langle \psi(\tau, p_1) | \psi(\tau, p_2) \rangle|^2, \quad (7)$$

$$\Delta_{\mathcal{F}}(p_1, p_2) = \mathcal{F}(p_1) - \mathcal{F}(p_2). \quad (8)$$

The intermediate regime with a limited amount of crosstalk is the most meaningful for the convergence study. In the limit of small  $r_G$ , the compiler produces as expected circuits with low fidelity and a convergence study in this regime does not require long-range interactions to the same extent as in the parameter regime suggested by us as  $r_s$  in Sec. I. The circuit in the limit of large  $r_G$  has no crosstalk and matches the GHZ state up to the accumulated errors of a CZ; this scenario does not challenge the convergence with regard to the bond dimension nor the radius  $r_H$ . Therefore, we check convergence for the  $8 \times 8$  grid for  $r_G = \sqrt{10}a$  as well as  $r_G = r_s = \sqrt{16}a$ , where both  $\mathcal{C}(p_1, p_2)$  and  $\Delta_{\mathcal{F}}(p_1, p_2)$  stay below a  $10^{-3}$  level for increasing the bond dimension  $\chi$  by fifty percent, decreasing the time step by a factor of 10, and increasing  $r_H$  by four lattice spacings  $a$ , except for one data point for  $r_G = \sqrt{10}a$ . One additional intermediate data point is shown for comparison. If we compare  $\mathcal{C}(p_1, p_2)$  and  $\Delta_{\mathcal{F}}(p_1, p_2)$  to the infidelities of Fig. 2b), the numerical error stays about one order of magnitude below the corresponding infidelities for  $r_G = \sqrt{10}a$  and  $r_G = \sqrt{16}a$ , respectively. Hence, we consider the results converged on the relevant order of magnitude and use  $\chi = 12$ ,  $dt = 0.001\mu\text{s}$ , and  $d_{\text{offset}} = 2a$  for all simulations.

TABLE I. *Convergence study for tensor networks.* We evaluate the convergence of the tensor network simulations as a function of the bond dimension  $\chi$ , the time step  $dt$ , and the radius  $r_H$  of the interactions included in the Hamiltonian. We focus on the overlap of the final states of simulations with respect to the parameters  $p_i$  that we check in convergence, i.e.,  $\mathcal{C}(p_1, p_2) = 1 - |\langle \psi(\tau, p_1) | \psi(\tau, p_2) \rangle|^2$ , and the induced change in the fidelity to the GHZ state, i.e.,  $\Delta_{\mathcal{F}}(p_1, p_2) = \mathcal{F}(p_1) - \mathcal{F}(p_2)$ . Distances are implicitly given in terms of the lattice spacing  $a$  and the time in  $\mu\text{s}$ . Recall that the perfect GHZ state serving as the target has a bond dimension of  $\chi = 2$ .

Convergence $\chi$	$r_G = \sqrt{10}a$	$r_G = \sqrt{16}a$
$\mathcal{C}(\chi = 12, \chi = 18)$	$0.43 \cdot 10^{-3}$	$0.13 \cdot 10^{-3}$
$\mathcal{C}(\chi = 15, \chi = 18)$	$0.48 \cdot 10^{-3}$	$0.10 \cdot 10^{-3}$
$\Delta_{\mathcal{F}}(\chi = 12, \chi = 18)$	$-0.05 \cdot 10^{-3}$	$-0.01 \cdot 10^{-3}$
$\Delta_{\mathcal{F}}(\chi = 15, \chi = 18)$	$0.26 \cdot 10^{-3}$	$-0.01 \cdot 10^{-3}$
Convergence $dt$	$r_G = \sqrt{10}a$	$r_G = \sqrt{16}a$
$\mathcal{C}(dt = 0.001, dt = 0.0001)$	$0.78 \cdot 10^{-3}$	$0.24 \cdot 10^{-3}$
$\mathcal{C}(dt = 0.005, dt = 0.0001)$	$0.80 \cdot 10^{-3}$	$0.23 \cdot 10^{-3}$
$\Delta_{\mathcal{F}}(dt = 0.001, dt = 0.0001)$	$0.20 \cdot 10^{-3}$	$0.12 \cdot 10^{-3}$
$\Delta_{\mathcal{F}}(dt = 0.005, dt = 0.0001)$	$0.31 \cdot 10^{-3}$	$0.08 \cdot 10^{-3}$
Convergence $r_H = r_G + d_{\text{offset}}$	$r_G = \sqrt{10}a$	$r_G = \sqrt{16}a$
$\mathcal{C}(d_{\text{offset}} = 2, d_{\text{offset}} = 6)$	$0.36 \cdot 10^{-3}$	$0.13 \cdot 10^{-3}$
$\mathcal{C}(d_{\text{offset}} = 4, d_{\text{offset}} = 6)$	$0.54 \cdot 10^{-3}$	$0.13 \cdot 10^{-3}$
$\Delta_{\mathcal{F}}(d_{\text{offset}} = 2, d_{\text{offset}} = 6)$	$1.5 \cdot 10^{-3}$	$0.25 \cdot 10^{-3}$
$\Delta_{\mathcal{F}}(d_{\text{offset}} = 4, d_{\text{offset}} = 6)$	$0.32 \cdot 10^{-3}$	$0.02 \cdot 10^{-3}$

#### IV. COMPILER FOR GLOBAL GHZ STATES

The compiler *RydberGHZ-C* compiles the algorithm for the global GHZ state preparation for the given constraints: the connectivity preventing gates within the radius  $r_G$ , the available gate set consisting of single-qubit rotations around the  $x$ -axis and the  $z$ -axis, and the CZ gate. We choose to implement a compiler from scratch due to the very specific target state and the parameters we need to tune, i.e., the distance  $r_G$  for parallel gates. Our compiler has two modes: the first mode outputs an algorithm with one initial Hadamard gate and a sequence of CNOT gates; the second mode targets directly a subset of native gates available on the digital twin of the Rydberg platform. We focus on the latter in the following, because the first mode is a special case of the second mode which is explained after the details of the algorithm.

The CNOT gate on a Rydberg platform can be executed as  $H_2 CZ_{1,2} H_2$  where the Hadamard gate  $H$  acts on the target atom [67]. We instead use the following decompositions for the Hadamard and CZ( $\phi$ ) gate obtained by a derivate of the open-source qoqo compiler adapted for the Rydberg platform [68]

$$H = R_z \left( \frac{\pi}{2} \right) R_x \left( \frac{\pi}{2} \right) R_z \left( \frac{\pi}{2} \right), \quad (9)$$

$$\begin{aligned} \text{CNOT} &= R_x^C(\pi) R_x^T \left( \frac{\pi}{2} \right) R_z^T \left( -\frac{\pi}{2} \right) R_x^T \left( \frac{\pi}{2} \right) CZ(\phi) \\ &R_z^C \left( \phi - \frac{3\pi}{2} \right) R_x^C(\pi) R_z^C \left( \frac{3\pi}{2} \right) \\ &R_z^T \left( -\phi - \frac{3\pi}{2} \right) R_x^T \left( \frac{\pi}{2} \right) R_z^T \left( \frac{3\pi}{2} \right). \end{aligned} \quad (10)$$

In practice, the experimental implementation of a CZ( $\phi$ ) gate represents the CZ gate up to single-qubit rotations [36]. The controlled-phase gate CZ( $\phi$ ) has therefore more gates in comparison to the previously mentioned decomposition of Ref. [67]. We distinguish the control qubit and the target qubit by a superscript «C» and «T», respectively.

Our approach to compiling the algorithm relies on the fact that all qubits are initially in the state  $|0\rangle$ ; moreover, any qubit already part of the GHZ state can act as a control qubit in an entangling gate to add qubits to the GHZ state multiple times. Figure 6a) summarizes the idea of how to parallelize the algorithm in a one-dimensional system reducing the circuit depth  $D$  to  $(L/2 + 1)$  for even  $L$ ; the benefit can be even larger in a two-dimensional square system where the circuit depth of  $L^2$  in the serial execution can be reduced to  $(L + 1)$  for even  $L$ . In both examples, we consider the Hadamard gate combined with CNOTs and no restriction on the number of parallel gates executed at the same time with a nearest-neighbor connectivity. The Rydberg platform has the lower bound of  $D_{\text{min}} = (3 + 5L)$  for even  $L$  and  $r_G = a$ ; due to  $r_G = a$ , this remains a theoretical lower bound without an acceptable fidelity [69]. The meaningful upper bound is an algorithm without any parallel CZ gates, while parallel local gates are allowed:  $D_{\text{CZ-serial}} = L^2 + 14$ . This upper bound is 30 and 78 for a  $4 \times 4$  and  $8 \times 8$  grid, respectively. The completely serial execution of all gates is  $D_{\text{serial}} = 11(L^2 - 1) + 3$ .

Our compiler lists all the possible intermediate configurations of a GHZ circuit up to a  $4 \times 4$  grid in a reasonable time. The number of intermediate configurations rapidly grows with increasing system sizes, which forces us to truncate the least promising configurations based on metrics defined in the following. The compiler without truncation contains the following steps:

1. Fix minimal distance  $r_G$ , i.e., the minimal distance between any two atoms participating in different CZ gates at the same time.
2. A set of unique sites is selected as initial starting points for the Hadamard gate and store them as a list of configurations  $\mathcal{C}_\gamma$ . No unique site inside the set maps via rotations or reflections of the grid to another site within the set.
3. List all possible pairs  $\mathcal{P}_\alpha$  of control and target sites for the configurations  $\mathcal{C}_\gamma$ .
4. List all sets  $\mathcal{S}_\beta$  of pairs  $\mathcal{P}_\alpha$  which can run in parallel while obeying the minimal distance  $r_G$ . Subsets are not included, e.g., if  $\mathcal{S}_\beta = (\mathcal{P}_A, \mathcal{P}_B, \mathcal{P}_D)$  is included, we omit  $\mathcal{S}_{\beta'} = (\mathcal{P}_A, \mathcal{P}_B)$ .
5. Create a new configuration  $\mathcal{C}'_\gamma$  for each  $\mathcal{S}_\beta$ . Check

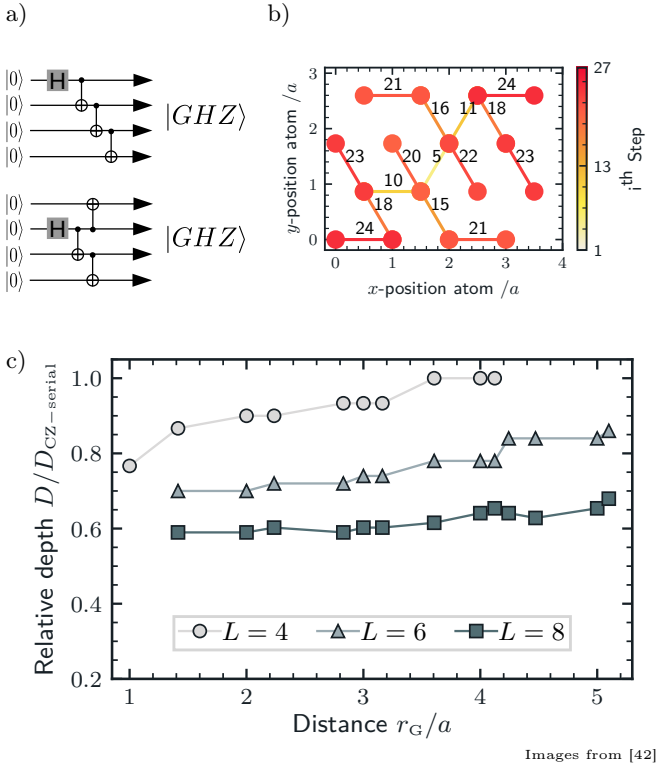


FIG. 6. *Circuit depth of a GHZ state preparation.* a) The upper circuit shows the serial preparation of the GHZ state in a one-dimensional geometry. The lower half sketches the parallel approach for the preparation of a one-dimensional system with nearest-neighbor connectivity and the algorithm follows a light cone starting in the middle and moving outwards. b) Example for a parallel preparation of the GHZ state in a  $4 \times 4$  hexagonal grid where the minimal distance between sites of two CZ gates is set to  $r_G = 2a$ . Links of the same color are CZ gates executed in parallel; the total circuit depth for the Rydberg platform is  $D = 27$ . The positions of the atoms are shown in terms of the lattice spacing  $a$ . c) Selecting a minimal distance  $r_G$  between the sites of two CZ gates to avoid the crosstalk of the Rydberg blockade leads to different circuit depths; truncations of intermediate states are set for all system sizes. We point out that the speed-up from a parallel execution grows with increasing system sizes.

if the new configuration  $\mathcal{C}'_\gamma$  is a solution.

6. Block the qubits involved in a CZ gate for the next four iterations to allow the application of the local gates for the Rydberg platform. Reduce iterations blocked for local operations by one for all qubits not involved in a CZ gate.
7. Continue with step 3) using the new configurations  $\mathcal{C}'_\gamma$  as  $\mathcal{C}_\gamma$ . Allow to truncate entries in  $\mathcal{C}_\gamma$  based on symmetry arguments or truncation rules.

The scaling of the number of intermediate configurations is kept to a minimum due to the exploitation of symmetries, e.g., step 2) generates only three unique configurations for a  $4 \times 4$  square lattice. The other configurations are rotations and reflections of those three configurations.

TABLE II. *Statistics for GHZ circuit.* Given a safe distance  $r_S = r_G$  to run CZ gates in parallel, we evaluate the circuit depth and number of single-qubit and two-qubit gates. In detail, we show the lower bound of the circuit depth  $D_{\min}$  at  $r_G = a$  for a nearest-neighbor connectivity, the actual circuit depth  $D(r_S)$ , the circuit depth with all CZ gates in serial  $D_{CZ-serial}$ , and the circuit depth with all gates in serial  $D_{serial}$ , i.e., the number of gates. Furthermore, we provide the average number  $O_1$  and  $O_2$  as well as the maximal number  $MAX_1$  and  $MAX_2$  per layer of one-qubit and two-qubit gates, respectively. These numbers for the choice of  $r_S$  give an estimate of the hardware requirements, e.g., in terms of laser power. Finally, the Quantum Gates per Second (QGS) enable a comparison across different platforms, where we present two scenarios with  $\tau_{Layer} = 200\text{ns}$  per layer and  $\tau_{Layer} = 2\mu\text{s}$ .

Circuit property	$4 \times 4$ (16)	$6 \times 6$ (36)	$8 \times 8$ (64)
$r_S$	$\sqrt{8}a$	$4a$	$4a$
$D_{\min}$	23	33	43
$D(r_S)$	28	39	50
$D_{CZ-serial}$	30	50	78
$D_{serial}$	168	388	696
$O_1(r_S)$	5.5	9.1	12.7
$O_2(r_S)$	0.5	0.9	1.3
$MAX_1(r_S)$	10	12	16
$MAX_2(r_S)$	2	3	4
QGS(0.2 $\mu\text{s}$ )	$30 \cdot 10^6$	$50 \cdot 10^6$	$70 \cdot 10^6$
QGS(2 $\mu\text{s}$ )	$3 \cdot 10^6$	$5 \cdot 10^6$	$7 \cdot 10^6$

Despite this effort throughout the algorithm, we require the truncation of configurations for larger system sizes.

The most convenient place for the truncation of configurations is step 7) before starting the next iteration. We assign each configuration to a bin according to the number of already entangled qubits and use it as the first criterion: we keep truncating the bin with the smallest number of qubits and the configurations therein as long as we keep a given percentage of configurations defined as a parameter. The second metric takes into account the geometry of the intermediate configuration. We consider a center-of-mass close to the center of the grid as favorable because all corners can be reached in an equal number of steps. Moreover, a configuration with a large average distance from its own center of mass is closer to the corners of the system and comes with a higher chance to run gates in parallel in the next step. The fraction of configurations resulting in the largest intermediate GHZ state is at least kept with respect to the previous configuration. An option for a more aggressive truncation keeps only the largest sets  $\mathcal{S}_\beta$  in step 4), which stays disabled for the Rydberg system.

Considering the compiler for the subset of native Rydberg gates, we point out how the first compiler mode in terms of a Hadamard gate and CNOT gates is working: consecutive CNOT gates can run without intermediate single-qubit gates, which results in setting the blocked cycles in step 6) to zero for RydberGHZ-C.

Figure 6c) compares the circuit depth as a function of

the distance  $r_G$  for different system sizes. The truncation of states during the search does not necessarily converge to the global minima. The compiler settings allow one to truncate up to fifty percent of the configurations if they have two or more qubits less in the GHZ state than the best configuration. Afterward, we keep 300 geometries with the best metrics. An example of the  $4 \times 4$  grid with minimal distance  $r_G = 2a$  is shown for the hexagonal lattice layout in Fig. 6b). The possible reduction of the circuit depth increases with the system size. For the circuits of Figs. 1, 2, and 4, we keep up to 600 geometries during compiling the algorithm.

The front end of the tensor network software takes care of scheduling the parallel pulses according to the compiler output, including the distance  $r_G$ . The scheduling includes here the individual addressing of the atoms, i.e., activating the pulses on the selected atoms and setting no laser-driving terms for atoms not involved in any gate. The pulses for the Rabi frequency  $\Omega^R$  driving the transition  $|1\rangle \leftrightarrow |r\rangle$  and the corresponding detuning are specified in Ref. [44], where the detuning follows a Gaussian shape and the Rabi frequency is 10 MHz. The total duration of a single CZ is  $0.122 \mu\text{s}$  and we choose the amplitudes for the single-qubit gates to match this duration of the CZ gate. The TTN simulation uses this a duration of  $0.122 \mu\text{s}$  independent from the scenarios for decoherence, i.e., the theoretical estimate for decoherence according to Eq. (6) with  $\tau_{\text{Layer}} = 0.2 \mu\text{s}$  and  $\tau_{\text{Layer}} = 2 \mu\text{s}$  is calculated in a post-processing step without accessing TTN results. However, the time  $\tau_{\text{Layer}}$  becomes a relevant variable of the platform as soon as we consider decoherence, recall Fig. 4d). We report selected key statistics of the circuits in Tab. II. Especially the  $8 \times 8$  grid demonstrates how larger system sizes profit from the parallelization with 35% speedup in comparison to a circuit serial in CZ gates as well as 92% speedup compared to a completely serial circuit. In contrast, we are only 15% above the theoretical minimum shown in Tab. II. The maximal number of local gates and CZ gates further gives an estimate of which laser power is required to execute gates in parallel. For cross-platform comparisons, the level of parallelization is only one aspect, but the gates executed per time unit are more meaningful. Hence, we also list the number of Quantum Gates per Second (QGS) for the two scenarios, e.g., the preparation of the global GHZ state on an  $8 \times 8$  grid in the more conservative scenario still runs approximately  $7 \cdot 10^6$  gates per second.

## V. CONCLUSION

We have analyzed the parallel execution of a quantum algorithm on the digital twin of a quantum computer. The simulation of an algorithm on the pulse level involving the Hamiltonian leads to valuable insights into the quantum hardware, e.g., in terms of qubit crosstalk. In detail, the numerical simulations analyze the influence of the Rydberg interactions on the parallel execution of

controlled-phase gates. We have simulated the qutrits physics in systems of up to a size of  $8 \times 8$  sites with a tree tensor network. The simulations cover a variety of effects, including decay effects modeled by a Lindblad channel and the remaining population in the Rydberg state, where the latter would require non-Markovian effects in a two-level open system description.

The focus on the preparation of a GHZ state explores one of the first standard demonstrations of control and stability of new quantum processors. We have shown that the circuit depth for the preparation of a GHZ state with almost 700 gates for an  $8 \times 8$  grid can be reduced by more than 35% percent under the constraint of avoiding parallel gates for a radius smaller than  $r_s = \sqrt{16}a$ . Satisfying this condition, the infidelity per single CZ gate in the closed Rydberg quantum system increases by one or two orders of magnitude in comparison to the infinite- $r_G$  limit. However, the final infidelity stays a factor of 5 to 10 below the major source of errors introduced by the decay from the Rydberg state. Furthermore, we have shown that the infidelity due to decay from the Rydberg state stays constant beyond a certain circuit depth. Dephasing, i.e., the next most important open quantum system effect, represents the incentive to minimize the circuit depth as long as the crosstalk is under control. Due to the speedup of 92% and the inherent reduction in decoherence revealed by the digital twin in comparison to a completely serial circuit, we identify quantum gate parallelism as a necessary pathway to maximize the performance of NISQ devices.

Building on this initial investigation, we foresee a number of important questions that now can and shall be addressed to support future NISQ development, along the lines of the three challenges for future quantum hardware outlined in the white paper [70]. For example, the development – also via optimal control methods [8, 10] – of a four-qubit gate performing two CZ gates with suppression of crosstalk could highly improve the system performance for Rydberg systems. We foresee an engineering challenge to design the embedded classical hardware to control and apply the laser pulses in parallel. Questions related to the green quantum advantage and how parallel execution can be leveraged to shift the boundary for energy-efficient computing more toward QPUs shall be addressed [71]. Moreover, Rydberg platforms offer two pathways to modify the connectivity. On the one hand, the Rydberg blockade radius can be modified which affects the range at which two-qubit gates are possible [72]. On the other hand, shift operations offer another degree of freedom: the Rydberg atoms trapped in the optical tweezers can be shifted during an algorithm as demonstrated in [32]. This additional degree of freedom can possibly be exploited to further improve algorithm efficiency.

The digital twin introduced here can be straightforwardly applied to different quantum computing hardware, such as superconducting or ion platforms. Several questions remain open on the theory side, such as

gaining a better understanding of the running details of other algorithms and platforms. For example, a detailed comparison of the highly parallelized GHZ state preparation in Ref. [73] is another intriguing direction, where the protocol uses auxiliary qubits and measurements. As is, our implementation of a digital twin is directly relevant for NISQ devices with the current number of simulated qubits. Different improvements on the software and hardware aspects of the digital twin, e.g., via parallelization on classical computers [74], will enable in the near future exploring higher entangling algorithms and larger system sizes.

*Acknowledgments* – We thank Marco Ballarin, Timo Felser, and Marco Trenti for their work on the underlying numerical library *Quantum TEA*; our partners from the QRydDemo project Hans Peter Büchler, Florian Meinert, Tilman Pfau, and Jürgen Stuhler for useful discussions; Marcello Dalmonte, Nora Reinić, and Ilaria Siloi for feedback. This project has received funding from the German Federal Ministry of Education and Research (BMBF)

under the funding program quantum technologies – from basic research to market – with the grant QRydDemo. We acknowledge support from the Italian Ministry of University and Research (MUR) via PRIN2022-TANQU and the Departments of Excellence grant 2023-2027 Quantum Frontiers; we acknowledge support from the European Union via H2020 projects Pasquans2, EU-RyQA and TEXTAROSSA, the EU-QuantERA projects QuantHEP and T-NISQ, the WCRI-Quantum Computing and Simulation Center of Padova University, and the Italian National Centre on HPC, Big Data and Quantum Computing. This work was performed in part at the Aspen Center for Physics, which is supported by National Science Foundation grant PHY-2210452; the participation of D. J. at the Aspen Center for Physics was supported by the Simons Foundation. The authors acknowledge support by the state of Baden-Württemberg through bwHPC and the German Research Foundation (DFG) through grant no INST 40/575-1 FUGG (JUSTUS 2 cluster).

- 
- [1] C. G. Almudever, L. Lao, X. Fu, N. Khammassi, I. Ashraf, D. Iorga, S. Varsamopoulos, C. Eichler, A. Wallraff, L. Geck, A. Kruth, J. Knoch, H. Bluhm, and K Bertels, “The engineering challenges in quantum computing,” in *Design, Automation & Test in Europe Conference & Exhibition (DATE), 2017* (2017) pp. 836–845.
- [2] Colin D. Bruzewicz, John Chiaverini, Robert McConnell, and Jeremy M. Sage, “Trapped-ion quantum computing: Progress and challenges,” *Applied Physics Reviews* **6**, 021314 (2019).
- [3] Koen Bertels, Aritra Sarkar, and Imran Ashraf, “Quantum computing—from NISQ to PISQ,” *IEEE Micro* **41**, 24–32 (2021).
- [4] Elijah Pelofske, Andreas Bärtschi, and Stephan Eidenbenz, “Quantum volume in practice: What users can expect from NISQ devices,” *IEEE Transactions on Quantum Engineering* **3**, 1–19 (2022).
- [5] John Preskill, “Quantum Computing in the NISQ era and beyond,” *Quantum* **2**, 79 (2018).
- [6] Pascal Cerfontaine, Tim Botzem, Julian Ritzmann, Simon Sebastian Humpohl, Arne Ludwig, Dieter Schuh, Dominique Bougeard, Andreas D. Wieck, and Hendrik Bluhm, “Closed-loop control of a gaas-based singlet-triplet spin qubit with 99.5% gate fidelity and low leakage,” *Nature Communications* **11**, 4144 (2020).
- [7] Zhiwen Zong, Zhenhai Sun, Zhangjingzi Dong, Chongxin Run, Liang Xiang, Ze Zhan, Qianlong Wang, Ying Fei, Yaozu Wu, Wenyan Jin, Cong Xiao, Zhilong Jia, Peng Duan, Jianlan Wu, Yi Yin, and Guoping Guo, “Optimization of a controlled-z gate with data-driven gradient-ascent pulse engineering in a superconducting-qubit system,” *Phys. Rev. Applied* **15**, 064005 (2021).
- [8] Christiane P. Koch, Ugo Boscain, Tommaso Calarco, Gunther Dirr, Stefan Filipp, Steffen J. Glaser, Ronnie Kosloff, Simone Montangero, Thomas Schulte-Herbrüggen, Dominique Sugny, and Frank K. Wilhelm, “Quantum optimal control in quantum technologies. strategic report on current status, visions and goals for research in europe,” *EPJ Quantum Technology* **9**, 19 (2022).
- [9] Frank K. Wilhelm, Susanna Kirchhoff, Shai Machnes, Nicolas Wittler, and Dominique Sugny, “An introduction into optimal control for quantum technologies,” arXiv e-prints 2003.10132 (2020).
- [10] Matthias M. Müller, Ressa S. Said, Fedor Jelezko, Tommaso Calarco, and Simone Montangero, “One decade of quantum optimal control in the chopped random basis,” *Reports on Progress in Physics* **85**, 076001 (2022).
- [11] Jutho Haegeman, Christian Lubich, Ivan Oseledets, Bart Vandereycken, and Frank Verstraete, “Unifying time evolution and optimization with matrix product states,” *Phys. Rev. B* **94**, 165116 (2016).
- [12] Daniel Jaschke, Simone Montangero, and Lincoln D. Carr, “One-dimensional many-body entangled open quantum systems with tensor network methods,” *Quantum Science and Technology* **4**, 013001 (2018).
- [13] Daniel Bauernfeind and Markus Aichhorn, “Time Dependent Variational Principle for Tree Tensor Networks,” *SciPost Phys.* **8**, 24 (2020).
- [14] Timo Felser, Simone Notarnicola, and Simone Montangero, “Efficient tensor network ansatz for high-dimensional quantum many-body problems,” *Phys. Rev. Lett.* **126**, 170603 (2021).
- [15] Thomas Häner and Damian S. Steiger, “0.5 Petabyte Simulation of a 45-qubit Quantum Circuit,” in *Proceedings of the International Conference for High Performance Computing, Networking, Storage and Analysis, SC ’17* (ACM, New York, NY, USA, 2017) pp. 33:1–33:10.
- [16] Thomas Häner, Damian S. Steiger, Krysta Svore, and Matthias Troyer, “A software methodology for compiling quantum programs,” *Quantum Science and Technology* **3**, 020501 (2018).
- [17] Luke E. Heyfron and Earl T. Campbell, “An efficient quantum compiler that reduces T count,” *Quantum Science and Technology* **4**, 015004 (2018).
- [18] Prakash Murali, Jonathan M. Baker, Ali Javadi-Abhari,

- Frederic T. Chong, and Margaret Martonosi, “Noise-adaptive compiler mappings for noisy intermediate-scale quantum computers,” in *Proceedings of the Twenty-Fourth International Conference on Architectural Support for Programming Languages and Operating Systems*, ASPLOS '19 (Association for Computing Machinery, New York, NY, USA, 2019) p. 1015–1029.
- [19] M. Saffman, T. G. Walker, and K. Mølmer, “Quantum information with Rydberg atoms,” *Rev. Mod. Phys.* **82**, 2313–2363 (2010).
- [20] Hendrik Weimer, Markus Müller, Igor Lesanovsky, Peter Zoller, and Hans Peter Büchler, “A Rydberg quantum simulator,” *Nature Physics* **6**, 382 (2010).
- [21] Robert Löw, Hendrik Weimer, Johannes Nipper, Jonathan B. Balewski, Björn Butscher, Hans Peter Büchler, and Tilman Pfau, “An experimental and theoretical guide to strongly interacting Rydberg gases,” *Journal of Physics B: Atomic, Molecular and Optical Physics* **45**, 113001 (2012).
- [22] M. Saffman, “Quantum computing with atomic qubits and Rydberg interactions: progress and challenges,” *Journal of Physics B: Atomic, Molecular and Optical Physics* **49**, 202001 (2016).
- [23] C. S. Adams, J. D. Pritchard, and J. P. Shaffer, “Rydberg atom quantum technologies,” *Journal of Physics B: Atomic, Molecular and Optical Physics* **53**, 012002 (2019).
- [24] Louis-Paul Henry, Slimane Thabet, Constantin Dalyac, and Loïc Henriët, “Quantum evolution kernel: Machine learning on graphs with programmable arrays of qubits,” *Phys. Rev. A* **104**, 032416 (2021).
- [25] Xiaoling Wu, Xinhui Liang, Yaoqi Tian, Fan Yang, Cheng Chen, Yong-Chun Liu, Meng Khoon Tey, and Li You, “A concise review of Rydberg atom based quantum computation and quantum simulation,” *Chinese Physics B* **30**, 020305 (2021).
- [26] T. M. Graham, M. Kwon, B. Grinkemeyer, Z. Marra, X. Jiang, M. T. Lichtman, Y. Sun, M. Ebert, and M. Saffman, “Rydberg-mediated entanglement in a two-dimensional neutral atom qubit array,” *Phys. Rev. Lett.* **123**, 230501 (2019).
- [27] Iyaylo S. Madjarov, Jacob P. Covey, Adam L. Shaw, Joonhee Choi, Anant Kale, Alexandre Cooper, Hannes Pichler, Vladimir Schkolnik, Jason R. Williams, and Manuel Endres, “High-fidelity entanglement and detection of alkaline-earth Rydberg atoms,” *Nature Physics* **16**, 857–861 (2020).
- [28] Iyaylo S. Madjarov, Jacob P. Covey, Adam L. Shaw, Joonhee Choi, Anant Kale, Alexandre Cooper, Hannes Pichler, Vladimir Schkolnik, Jason R. Williams, and Manuel Endres, “Author correction: High-fidelity entanglement and detection of alkaline-earth Rydberg atoms,” *Nature Physics* **17**, 144–144 (2021).
- [29] Xiao-Feng Shi, “Quantum logic and entanglement by neutral Rydberg atoms: methods and fidelity,” *Quantum Science and Technology* **7**, 023002 (2022).
- [30] Henning Labuhn, Sylvain Ravets, Daniel Barredo, Lucas Béguin, Florence Nogrette, Thierry Lahaye, and Antoine Browaeys, “Single-atom addressing in microtraps for quantum-state engineering using Rydberg atoms,” *Phys. Rev. A* **90**, 023415 (2014).
- [31] Antoine Browaeys and Thierry Lahaye, “Many-body physics with individually controlled Rydberg atoms,” *Nature Physics* **16**, 132–142 (2020).
- [32] Dolev Bluvstein, Harry Levine, Giulia Semeghini, Tout T. Wang, Sepehr Ebadi, Marcin Kalinowski, Alexander Keesling, Nishad Maskara, Hannes Pichler, Markus Greiner, Vladan Vuletić, and Mikhail D. Lukin, “A quantum processor based on coherent transport of entangled atom arrays,” *Nature* **604**, 451–456 (2022).
- [33] M. Morgado and S. Whitlock, “Quantum simulation and computing with Rydberg-interacting qubits,” *AVS Quantum Science* **3**, 023501 (2021).
- [34] Sepehr Ebadi, Tout T. Wang, Harry Levine, Alexander Keesling, Giulia Semeghini, Ahmed Omran, Dolev Bluvstein, Rhine Samajdar, Hannes Pichler, Wen Wei Ho, Soonwon Choi, Subir Sachdev, Markus Greiner, Vladan Vuletić, and Mikhail D. Lukin, “Quantum phases of matter on a 256-atom programmable quantum simulator,” *Nature* **595**, 227–232 (2021).
- [35] Pascal Scholl, Michael Schuler, Hannah J. Williams, Alexander A. Eberharter, Daniel Barredo, Kai-Niklas Schymik, Vincent Lienhard, Louis-Paul Henry, Thomas C. Lang, Thierry Lahaye, Andreas M. Läuchli, and Antoine Browaeys, “Quantum simulation of 2D antiferromagnets with hundreds of Rydberg atoms,” *Nature* **595**, 233–238 (2021).
- [36] Harry Levine, Alexander Keesling, Giulia Semeghini, Ahmed Omran, Tout T. Wang, Sepehr Ebadi, Hannes Bernien, Markus Greiner, Vladan Vuletić, Hannes Pichler, and Mikhail D. Lukin, “Parallel implementation of high-fidelity multiqubit gates with neutral atoms,” *Phys. Rev. Lett.* **123**, 170503 (2019).
- [37] Thomas Monz, Philipp Schindler, Julio T. Barreiro, Michael Chwalla, Daniel Nigg, William A. Coish, Maximilian Harlander, Wolfgang Hänsel, Markus Hennrich, and Rainer Blatt, “14-qubit entanglement: Creation and coherence,” *Phys. Rev. Lett.* **106**, 130506 (2011).
- [38] Diogo Cruz, Romain Fournier, Fabien Gremion, Alix Jeannerot, Kenichi Komagata, Tara Tosić, Jarla Thiesbrummel, Chun Lam Chan, Nicolas Macris, Marc-André Dupertuis, and Clément Javerzac-Galy, “Efficient quantum algorithms for GHZ and W states, and implementation on the IBM quantum computer,” *Advanced Quantum Technologies* **2**, 1900015 (2019).
- [39] A. Omran, H. Levine, A. Keesling, G. Semeghini, T. T. Wang, S. Ebadi, H. Bernien, A. S. Zibrov, H. Pichler, S. Choi, J. Cui, M. Rossignolo, P. Rembold, S. Montangero, T. Calarco, M. Endres, M. Greiner, V. Vuletić, and M. D. Lukin, “Generation and manipulation of Schrödinger cat states in Rydberg atom arrays,” *Science* **365**, 570–574 (2019).
- [40] Gary J. Mooney, Gregory A. L. White, Charles D. Hill, and Lloyd C. L. Hollenberg, “Generation and verification of 27-qubit Greenberger-Horne-Zeilinger states in a superconducting quantum computer,” *Journal of Physics Communications* **5**, 095004 (2021).
- [41] T. M. Graham, Y. Song, J. Scott, C. Poole, L. Phuttitarn, K. Jooya, P. Eichler, X. Jiang, A. Marra, B. Grinkemeyer, M. Kwon, M. Ebert, J. Cherek, M. T. Lichtman, M. Gillette, J. Gilbert, D. Bowman, T. Ballance, C. Campbell, E. D. Dahl, O. Crawford, N. S. Blunt, T. Rogers, B. and Noel, and M. Saffman, “Multi-qubit entanglement and algorithms on a neutral-atom quantum computer,” *Nature* **604**, 457–604 (2021).
- [42] Daniel Jaschke, Alice Pagano, Sebastian Weber, and Simone Montangero, “Figures and supplemental material for “Ab-initio two-dimensional digital twin for quantum

- computer benchmarking (version 2)", (2022), supplemental materials contain the figures of the manuscript, additional figures, data for the figures, the quantum circuits used in the simulations as figures and json-files, and various digital twin sketches.
- [43] Sven Jandura and Guido Pupillo, "Time-Optimal Two- and Three-Qubit Gates for Rydberg Atoms," *Quantum* **6**, 712 (2022).
- [44] Alice Pagano, Sebastian Weber, Daniel Jaschke, Tilman Pfau, Florian Meinert, Simone Montangero, and Hans Peter Büchler, "Error budgeting for a controlled-phase gate with strontium-88 Rydberg atoms," *Phys. Rev. Research* **4**, 033019 (2022).
- [45] Raymond Laflamme, Cesar Miquel, Juan Pablo Paz, and Wojciech Hubert Zurek, "Perfect quantum error correcting code," *Phys. Rev. Lett.* **77**, 198–201 (1996).
- [46] A. M. Steane, "Simple quantum error-correcting codes," *Phys. Rev. A* **54**, 4741–4751 (1996).
- [47] Daniel Gottesman, "An introduction to quantum error correction," in *Proceedings of Symposia in Applied Mathematics – Quantum Computation: A Grand Mathematical Challenge for the Twenty-First Century and the Millennium*, Vol. 58 (2002) pp. 221–236.
- [48] Pietro Silvi, Ferdinand Tschirsich, Matthias Gerster, Johannes Jünemann, Daniel Jaschke, Matteo Rizzi, and Simone Montangero, "The Tensor Networks Anthology: Simulation techniques for many-body quantum lattice systems," *SciPost Phys. Lect. Notes*, 8 (2019).
- [49] Ulrich Schollwöck, "The density-matrix renormalization group in the age of matrix product states," *Annals of Physics* **326**, 96 – 192 (2011), January 2011 Special Issue.
- [50] Román Orús, "A practical introduction to tensor networks: Matrix product states and projected entangled pair states," *Annals of Physics* **349**, 117 – 158 (2014).
- [51] Simone Montangero, *Introduction to Tensor Network Methods* (Springer, 2018).
- [52] Mari Carmen Bañuls, "Tensor network algorithms: A route map," *Annual Review of Condensed Matter Physics* **14**, 173–191 (2023).
- [53] Siyuan Niu and Aida Todri-Sanial, "Effects of dynamical decoupling and pulse-level optimizations on ibm quantum computers," *IEEE Transactions on Quantum Engineering* **3**, 1–10 (2022).
- [54] Kenneth R. Brown, Jungsang Kim, and Christopher Monroe, "Co-designing a scalable quantum computer with trapped atomic ions," *npj Quantum Information* **2**, 16034 (2016).
- [55] James R. Wootton and Daniel Loss, "Repetition code of 15 qubits," *Phys. Rev. A* **97**, 052313 (2018).
- [56] Alpha Gaëtan, Yevhen Miroshnychenko, Tatjana Wilk, Amodsen Chotia, Matthieu Viteau, Daniel Comparat, Pierre Pillet, Antoine Browaeys, and Philippe Grangier, "Observation of collective excitation of two individual atoms in the Rydberg blockade regime," *Nature Physics* **5**, 115–118 (2009).
- [57] E. Urban, T. A. Johnson, T. Henage, L. Isenhower, D. D. Yavuz, T. G. Walker, and M. Saffman, "Observation of Rydberg blockade between two atoms," *Nature Physics* **5**, 110–114 (2009).
- [58] Andrew J. Daley, "Quantum trajectories and open many-body quantum systems," *Advances in Physics* **63**, 77–149 (2014).
- [59] "The first step of quantum trajectories relies on the non-hermitian evolution of the quantum system which causes a drop in the norm. For each trajectory, a random number  $r$  is drawn and a jump is applied as soon as the norm drops below  $r$ . In our case, we are interested in the probability of such an event, but we are not considering recovering decaying states after the jump. Thus, we have no additional benefit of averaging over trajectories which all lead to a zero fidelity with the GHZ states as they have at least one qubit in the state  $|d\rangle$  outside the computational basis of the qubit. In summary, the lost norm is sufficient to obtain the percentage of incorrect preparations."
- [60] Gang Li, Yali Tian, Wei Wu, Shaokang Li, Xiangyan Li, Yanxin Liu, Pengfei Zhang, and Tiancai Zhang, "Triply magic conditions for microwave transition of optically trapped alkali-metal atoms," *Phys. Rev. Lett.* **123**, 253602 (2019).
- [61] F. Meinert, T. Pfau, and C. Hölzl, "Quantum computing device, use, and method," (2021), EU Patent Application No. EP20214187.5.
- [62] Marco Ballarín, *Quantum Computer Simulation via Tensor Networks*, Master's thesis, Università degli Studi di Padova (2021).
- [63] "Quantum TEA: Quantum Tensor-network Emulator Applications," [https://baltig.infn.it/quantum\\_tea](https://baltig.infn.it/quantum_tea), last visited August 29th 2022.
- [64] Giovanni Cataldi, Ashkan Abedi, Giuseppe Magnifico, Simone Notarnicola, Nicola Dalla Pozza, Vittorio Giovannetti, and Simone Montangero, "Hilbert curve vs Hilbert space: exploiting fractal 2D covering to increase tensor network efficiency," *Quantum* **5**, 556 (2021).
- [65] Timo Felser, *Tree tensor networks for high-dimensional quantum systems and beyond*, Ph.D. thesis, Universität des Saarlands (2021).
- [66] Daniel Jaschke and Lincoln D. Carr, "Open source matrix product states: exact diagonalization and other entanglement-accurate methods revisited in quantum systems," *Journal of Physics A: Mathematical and Theoretical* **51**, 465302 (2018).
- [67] Loïc Henriët, Lucas Beguin, Adrien Signoles, Thierry Lahaye, Antoine Browaeys, Georges-Olivier Reymond, and Christophe Jurczak, "Quantum computing with neutral atoms," *Quantum* **4**, 327 (2020).
- [68] Nicolas Vogt, Kirsten Bark, Marina Walt, Sebastian Zanker, Jan-Michael Reiner, and Matteo Lodi, "qoco compiler," .
- [69] "The theoretical bound for the circuit depth assumes CZ running gates on nearest-neighbors, i.e., the control qubit of the first CZ gate can have its target qubit as left neighbor, while its right neighbor is the control qubit of a second CZ gate. This approach leads unavoidable to crosstalk as there are no means for this control qubit to distinguish which nearest-neighbor is the target qubit in its CZ gate. As the CZ gate is symmetric for the control and target qubit, the case of having the target qubit of another CZ as a nearest-neighbor leads to the same error."
- [70] Andrew Wack, Hanhee Paik, Ali Javadi-Abhari, Petar Jurcevic, Ismael Faro, Jay M. Gambetta, and Blake R. Johnson, "Quality, speed, and scale: three key attributes to measure the performance of near-term quantum computers," arXiv2110.14108 (2021).
- [71] Daniel Jaschke and Simone Montangero, "Is quantum computing green? an estimate for an energy-efficiency quantum advantage," *Quantum Science and Technology*

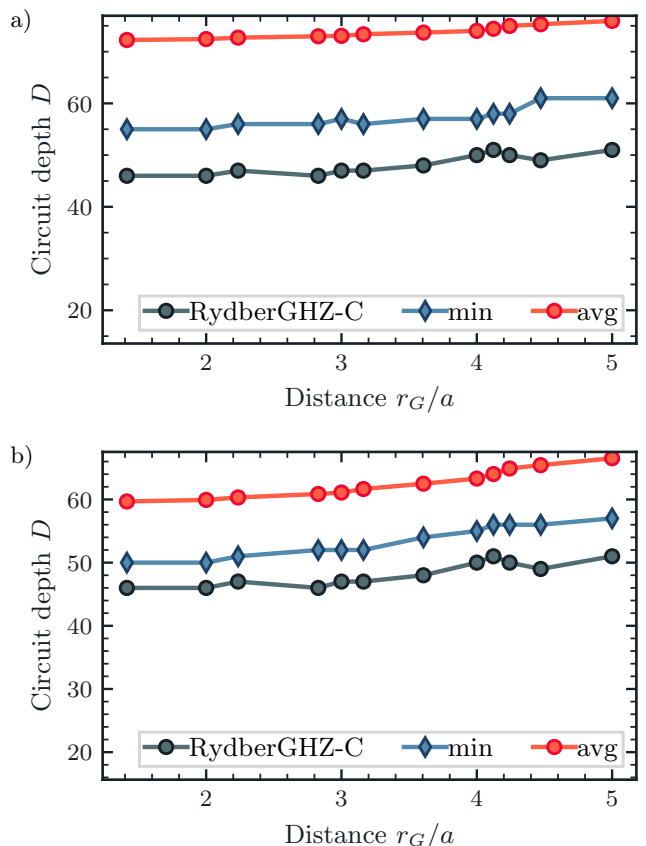
- 8, 025001 (2023).
- [72] David C. Spierings, Edwin Tham, Aharon Brodutch, and Ilya Khait, “Preferred interaction ranges in neutral-atom arrays in the presence of noise,” arXiv e-prints 2209.09234 (2022).
- [73] Lorenzo Piroli, Georgios Styliaris, and J. Ignacio Cirac, “Quantum circuits assisted by local operations and classical communication: Transformations and phases of matter,” *Phys. Rev. Lett.* **127**, 220503 (2021).
- [74] Paul Secular, Nikita Gourianov, Michael Lubasch, Sergey Dolgov, Stephen R. Clark, and Dieter Jaksch, “Parallel time-dependent variational principle algorithm for matrix product states,” *Phys. Rev. B* **101**, 235123 (2020).
- [75] Gushu Li, Yufei Ding, and Yuan Xie, “Tackling the qubit mapping problem for nisq-era quantum devices,” in *Proceedings of the Twenty-Fourth International Conference on Architectural Support for Programming Languages and Operating Systems*, ASPLOS ’19 (Association for Computing Machinery, New York, NY, USA, 2019) p. 1001–1014.

### Appendix A: Algorithms for compiling and scheduling GHZ states

We require a compiler minimizing the final circuit depth for the given constraint of crosstalk induced by an interaction decaying with the distance between the qubits. The minimization of the depth – not the number of gates – and the specific constraints are up to our knowledge not easily accessible in current software solutions. We encounter the problem to account for a) a figure of merit that minimizes the circuit depth of a parallel circuit, and b) blocking atoms around an atom executing a CZ gate for a given radius.

The focus of compilers is so far on minimizing the number of gates, which minimizes the circuit depth of a serial circuit; for example, implementations like SABRE tackle this problem [75]. To generate an  $N$ -qubit GHZ state, we need exactly  $N - 1$  entangling gates, which is already the optimum. We require a way to minimize the depth of a parallel circuit. Thus, one option to make this way work is to define multi-qubit gates as native gates that encode two, three, or even more CZ gates. For example, the native gate encoding two CZ gates is  $CZCZ_{ijkl} = CZ_{ij}CZ_{kl}$  where  $i, j, k, l$  encode the position of the atoms. Given the assumption that a compiler can translate between native gates given the corresponding rules, we have to define a large number of gates for larger systems with  $N$  atoms, e.g.,  $N(N - 1)/2$  starting with the pairs of CZ gates. These large number of gates likely lead to an unfavorable scaling when optimizing the problem.

The second option is then to go via the CZ gate as a native gate and use the connectivity given by compilers. The connectivity or coupling map of a QPU informs the compiler about which pairs of qubits can be used in an entangling gate without swap operations. Before adding the first CZ gate to a layer, the map starts with all nearest-neighbor connections; After adding a CZ gate, the map would have to be updated dynamically during compila-



Images from [42]

FIG. 7. *Benchmarking the RydberGHZ-C against random configurations for  $8 \times 8$  square lattice.* We compare the results of the RydberGHZ-C against the average (avg) circuit depth of 1000 randomized realizations of the circuit and the minimum circuit depth out of the random set. a) Random sequence of CNOT gates with the initial Hadamard gate placed in the middle of the circuit. b) Random sequence of CNOT gates with the initial Hadamard gate placed in the middle of the circuit and a waiting period of four cycles between CNOT gates. The waiting period is useful for accounting for the four local gates which have to run in between two CZ gates with the given native gate set.

tion for building each parallel layer. Another possible option is to pass a set of possible coupling maps that can be used for each parallel layer, but here we face a large set of possibilities that does not scale well with system size.

Each of the above modifications for the compiler require a significant modification of existing approaches. For these reasons, we aim for an algorithm which can minimize the circuit depth of the parallel GHZ state preparation on the Rydberg platform and serves as a compiler for our simulations. Figure 7 serves as a benchmark that the compilation is meaningful, where we consider two scenarios for an  $8 \times 8$  square lattice. First, we consider a circuit with the initial Hadamard gate in the center of the square lattice and then draw 1000 random



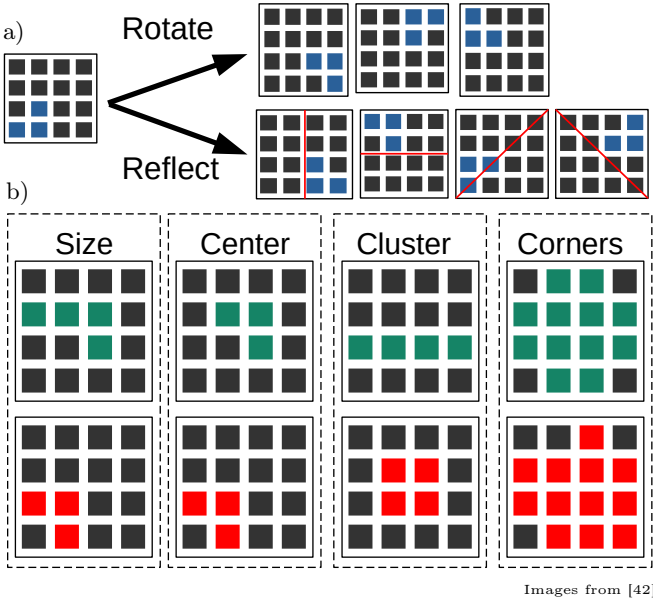


FIG. 8. *Building blocks for compiling the algorithms.* a) Symmetries lead to configurations which are equal by rotations or reflections; only one of them has to be kept for further steps. b) Truncation rules assign priority to more promising configurations (shown in green) over less promising configurations (shown in red). The rules consider the current size in the intermediate GHZ state, how close the center of mass is to the center, if the current sites form a cluster where all sites are within a small radius, and the size of the remaining corners.

sequences of the CNOT gates, see Fig. 7a). An important step in the compiler algorithm is the consideration of four local gates which are placed in between two CZ from the perspective of a single qubit; the condition can also be easily implemented here: if other qubits are available for an entangling gate, qubits are blocked for four cycles after each entangling gate and we draw the next step from the remaining possible options. This rule significantly improves the circuit depth of the best out of 1000 random sequences as shown in Fig. 7b), but the actual compiler still has a small advantage. Especially the second comparison which already has two key features of the optimal solution encoded, i.e., the central starting point and the consideration of the four local gates, confirms that the compilation is meaningful and we explain the approach now in more detail.

We recall the compiler steps from Sec. IV:

1. Fix minimal distance  $r_G$ , i.e., the minimal distance between any two atoms participating in different CZ gates at the same time.
2. A set of unique sites is selected as initial starting points for the Hadamard gate and store them as a list of configurations  $\mathcal{C}_\gamma$ . No unique site inside the set maps via rotations or reflections of the grid to

another site within the set, see Fig. 8a).

3. List all possible pairs  $\mathcal{P}_\alpha$  of control and target sites for the configurations  $\mathcal{C}_\gamma$ .
4. List all sets  $\mathcal{S}_\beta$  of pairs  $\mathcal{P}_\alpha$  which can run in parallel while obeying the minimal distance  $r_G$ . Subsets are not included, e.g., if  $\mathcal{S}_\beta = (\mathcal{P}_A, \mathcal{P}_B, \mathcal{P}_D)$  is included, we omit  $\mathcal{S}_{\beta'} = (\mathcal{P}_A, \mathcal{P}_B)$ .
5. Create a new configuration  $\mathcal{C}'_\gamma$  for each  $\mathcal{S}_\beta$ . Check if the new configuration  $\mathcal{C}'_\gamma$  is a solution.
6. Block the qubits involved in a CZ gate for the next four iterations to allow the application of the local gates for the Rydberg platform. Reduce iterations blocked for local operations by one for all qubits not involved in a CZ gate.
7. Continue with step 3) using the new configurations  $\mathcal{C}'_\gamma$  as  $\mathcal{C}_\gamma$ . Allow to truncate entries in  $\mathcal{C}_\gamma$  based on symmetry arguments or truncation rules, see Fig. 8.

The second step and the comment regarding the rotations and reflections are shown in detail in Fig. 8a): for the example of a  $4 \times 4$  grid, we show the three rotations and four reflections considered during the compilation to eliminate redundant solutions. The illustration shows the three relevant sites for the initial Hadamard gate in blue and how these three sites cover all configurations with the rotations and reflections. The equal approach can be carried out at later stages to find unique sets of configurations.

Figure 8b) sketches the rules to truncate configurations in step 7). The selection is implemented following four conditions. The first condition simply counts the number of qubits already added to an intermediate GHZ state after a given number of parallel layers, where we favor configurations that already have more qubits in the intermediate GHZ states, see label "Size". As mentioned before, the initial Hadamard gate close to the center is favorable for reaching all corners in the system in an equal number of steps; therefore, we generalize this premise and calculate the center of mass of the intermediate GHZ state and prefer states where the center of mass is close to the center of the grid ("Center"). The next condition is more subtle and concerns the chance to run CZ gates in parallel in the next layers: configurations arranged in a cluster likely fit in one or a few circles of radius  $r_G$ , while widely spread configurations cannot be easily covered by a few circles of the same radius. Thus, a higher standard deviation or mean distance from the center of mass of a configuration is beneficial for scheduling the next set of parallel CZ gates, see "Cluster". The fourth condition is the inverse of the third and avoids that there remains a large corner outside the GHZ state which cannot be finalized efficiently at the end, i.e., the "Corner" rule. Together, these four rules on the size, center, cluster, and corners decide on which configurations are kept for the next iteration. With many configurations truncated, this truncation leads to noise in the circuit depth as seen in Fig. 2b): even with a larger distance  $r_G$  enforced, we find a lower circuit depth than for smaller distances  $r_G$ .